LABORATORY STUDY OF SHEAR STRENGTH OF

FRACTURES IN SATURATED SANDSTONE

Pittawat Liabkrathok

A Thesis Submitted in Partial Fulfillment of the Requirements for the

Degree of Master of Engineering in Civil, Transportation

and Geo-resources Engineering

Suranaree University of Technology

Academic Year 2018

การศึกษาในห้องปฏิบัติการของกำลังเฉือนของรอยแตกใน
หินทรายอิ่มตัวด้วยน้ำ

นายพิทวัส เลียบกระโทก

LABORATORY STUDY OF SHEAR STRENGTH OF

FRACTURES IN SATURATED SANDSTONE

Suranaree University of Technology has approved this thesis submitted in partial fulfillment of the requirements for a Master's Degree.

Thesis Examining Committee

_____

(Asst. Prof. Dr. Akkhapun Wannakomol)

Chairperson

_____

(Prof. Dr. Kittitep Fuenkajorn)

Member (Thesis Advisor)

_____

(Assoc. Prof. Dr. Pornkasem Jongpradist)

Member

_____

(Prof. Dr. Santi Maensiri)

Vice Rector for Academic Affairs

and Internationalization

_____

(Assoc. Prof. Flt. Lt. Dr. Kontorn Chamniprasart)

Dean of Institute of Engineering

พิทวัส เลียบกระโทก : การศึกษาในห้องปฏิบัติการของกำลังเฉือนของรอยแตกในหิน
ทรายอิ่มตัวด้วยน้ำ (LABORATORY STUDY OF SHEAR STRENGTH OF
FRACTURES IN SATURATED SANDSTONE) อาจารย์ที่ปรึกษา : ศาสตราจารย์
ดร.กิตติเทพ เฟื่องขจร, 72 หน้า.

วัตถุประสงค์ของการศึกษาคือ เพื่อประเมินเชิงทดลองถึงผลกระทบของความอิ่มตัวด้วย
น้ำและความดันล้อมรอบต่อกำลังเฉือนและการขยายตัวของรอยแตกที่เกิดจากแรงดึงและการตัด
ผิวเรียบในหินทรายชุดพระวิหาร โครงให้แรงในหลายแกนถูกใช้เพื่อให้แรงดันล้อมรอบระหว่าง
1 ถึง 18 เมกะปาสคาล ด้วยความเร็วในการเฉือนผันแปรจาก 1.15×10^{-5} ถึง 1.15×10^{-2} มิลลิเมตรต่อ
วินาที ผลการทดสอบระบุว่าความอิ่มตัวด้วยน้ำสามารถลดกำลังเฉือนสูงสุดและกำลังเฉือนคงเหลือ
บนรอยแตก ความต้านทานการเฉือนของรอยแตกผิวเรียบมีแนวโน้มที่ไม่ขึ้นกับความเร็วในการ
เฉือนและความอิ่มตัวด้วยน้ำ ภายใต้แต่ละความเค้นล้อมรอบกำลังเฉือนสูงสุดกำลังเฉือนคงเหลือ
และอัตราการขยายตัวของรอยแตกผิวขรุขระมีค่าเพิ่มขึ้นเมื่อความเร็วในการเฉือนเพิ่มขึ้น พื้นที่ถูก
เฉือนเพิ่มขึ้นเมื่อความดันล้อมรอบเพิ่มขึ้นและความเร็วในการเฉือนลดลง เกณฑ์เชิงประจักษ์ที่รวม
ผลกระทบของความเร็วในการเฉือนไว้อย่างชัดเจน ได้ถูกนำเสนอเพื่อใช้อธิบายกำลังเฉือนสูงสุด
และกำลังเฉือนคงเหลือของรอยแตกในหินทรายที่อิ่มตัวด้วยน้ำ เกณฑ์ดังกล่าวสอดคล้องดีกับผล
การทดสอบซึ่งอาจใช้ในการคาดคะเนกำลังเฉือนของรอยแตกของหินทรายที่อิ่มตัวด้วยน้ำภายใต้
สภาวะความเค้นในภาคสนาม

สาขาวิชา เทคโนโลยีธรณี   ลายมือชื่อนักศึกษา _พิทวัส เลียบกระโทก_

ปีการศึกษา 2561   ลายมือชื่ออาจารย์ที่ปรึกษา _น. _____

PITTAWAT LIABKRATHOK : LABORATORY STUDY OF SHEAR

STRENGTH OF FRACTURES IN SATURATED SANDSTONE.

THESIS ADVISOR : PROF. KITTITEP FUENKAJORN, Ph.D., P.E., 72 PP.

DISPLACEMENT VELOCITY/SHEAR STRENGTH/DILATION/ROCK

FEACTURE/SATURATION.

The objective of this study is to experimentally determine the effects of water saturation and confining pressure on shear strengths and dilations of tension-induced and smooth saw-cut fractures prepared in Phra Wihan sandstone. A polyaxial load frame is used to apply confining pressures between 1 to 18 MPa with shear velocities ranging from 1.15×10^{-5} to 1.15×10^{-2} mm/s. The results indicate that water saturation can reduce the peak and residual shear strengths on the fractures. Shearing resistances of smooth saw-cut surfaces tend to be independent on the shear velocity and water saturation. Under each confinement the peak and residual shear strengths and dilation rates of rough fractures increase with shear velocities. The sheared-off areas increase when the confining pressure increases, and the shear velocity decreases. An empirical criterion that explicitly incorporates the effects of shear velocity is proposed to describe the peak and residual shear strengths of fractures in saturated sandstone. The criterion fits well to the test results, which may be used to predict the shear strengths of fracture of the saturated sandstone under in-situ condition.

School of Geotechnology

Academic Year 2018

Student's Signature พิทวัส เลียบกระโทก

Advisor's Signature

ACKNOWLEDGMENTS

I would like to express my sincere thanks to Prof. Dr. Kittitep Fuenkajorn for his valuable guidance and efficient supervision. I appreciate his strong support, encouragement, suggestions and comments during the research period. My heartiness thanks to Dr. Supattra Khamrat and Dr. Thanittha Thongprapha for their constructive advice, valuable suggestions and comments on my research works as thesis committee members. Grateful thanks are given to all staffs of Geomechanics Research Unit, Institute of Engineering who supported my work.

Finally, I would like to thank beloved parents for their love, support and encouragement.
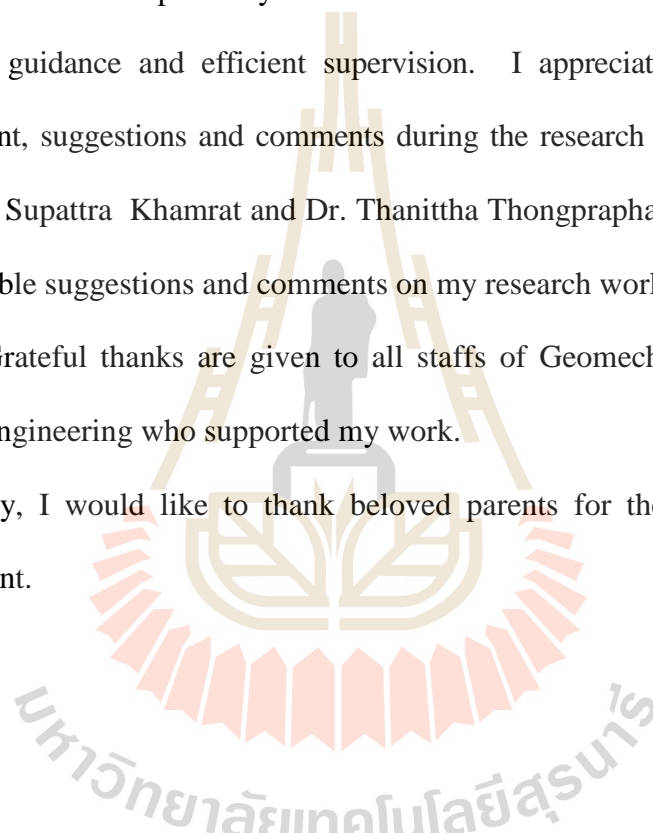
Pittawat Liabkrathok

TABLE OF CONTENTS

Page

TABLE OF CONTENTS (Continued)

TABLE OF CONTENTS (Continued)

Page

LIST OF TABLES

LIST OF FIGURES

LIST OF FIGURES (Continued)

LIST OF FIGURES (Continued)

LIST OF FIGURES (Continued)

SYMBOLS AND ABBREVIATIONS

α = Empirical parameters

β = Angle between σ_1 and σ_n axis

γ_{oct} = Octahedral shear strain

δ = Empirical parameters

ε_m = Mean strain

η = Empirical constant

θ = Angle

ι = Empirical constant

λ = Empirical parameter

ξ = Empirical constant

σ = Normal stress

σ_1 = Major principal stress

$\sigma_{1,f}$ = Major principal stress at failure

$\sigma_{1,P}$ = Major principal stress at peak

$\sigma_{1,R}$ = Major principal stress at residual

σ_2 = Intermediate stress

σ_3 = Minor principal stress

σ_c = Uniaxial compressive strength

$\sigma_{c,dry}$ = Uniaxial compressive strength under dry condition

SYMBOLS AND ABBREVIATIONS (Continued)

$\sigma_{c,sat}$ = Uniaxial compressive strength under saturated condition

σ_m = Mean stress

σ_n = Normal stress

σ_{n0} = Initial normal stress

σ_o = Lateral stress that is parallel to the fracture plane

σ_{oct} = Octahedral normal stress

σ_p = Lateral stress that is normal to the fracture plane

τ = Shear strength

τ_f = Shear strength at peak

τ_{oct} = Octahedral shear stress

τ_r = Residual shear strength

τ_s = Shear strength of saw-cut

τ_{xx} = Shear stress on the x plane due to a force acting in the x direction

τ_{xy} = Shear stress on the x plane due to a force acting in the y direction

τ_{yy} = Shear stress on the y plane due to a force acting in the y direction

φ = Empirical constant

ω = Empirical constant

$\partial\sigma_1/\partial t$ = Loading rate

ϕ = Friction angle

ϕ_b = Basic friction angle

SYMBOLS AND ABBREVIATIONS (Continued)

ϕ_r	=	Residual friction angle
ϖ	=	Empirical constant
a	=	Empirical constant
b	=	Empirical parameter
c	=	Cohesion
c_a	=	Apparent cohesion
CNL	=	Constant normal load
CNS	=	Constant normal stiffness
d_1	=	Vertical displacement
d_3	=	Lateral displacement
$d_{3,c}$	=	Calculated lateral displacement
$d_{3,m}$	=	Vertical movement of steel beam / 12
d_n	=	Normal displacement
d_n/d_s	=	Dilation rate
d_s	=	Shear displacement
$\dot{d}_1$	=	Axial displacement rate
$\dot{d}_s$	=	Shear displacement rate
E_{dry}	=	Young's modulus under dry condition
E_{sat}	=	Young's modulus under saturated condition
E_{sec}	=	Secant Young's modulus
E_{tan}	=	Tangent Young's modulus

SYMBOLS AND ABBREVIATIONS (Continued)

i	=	Angle of inclination of the first order
JRC	=	Joint roughness coefficient
S_0	=	Cohesion of the surface
w	=	Water content
w_{ave}	=	Average water content
W_d	=	Distortional strain energy
W_m	=	Mean strain energy
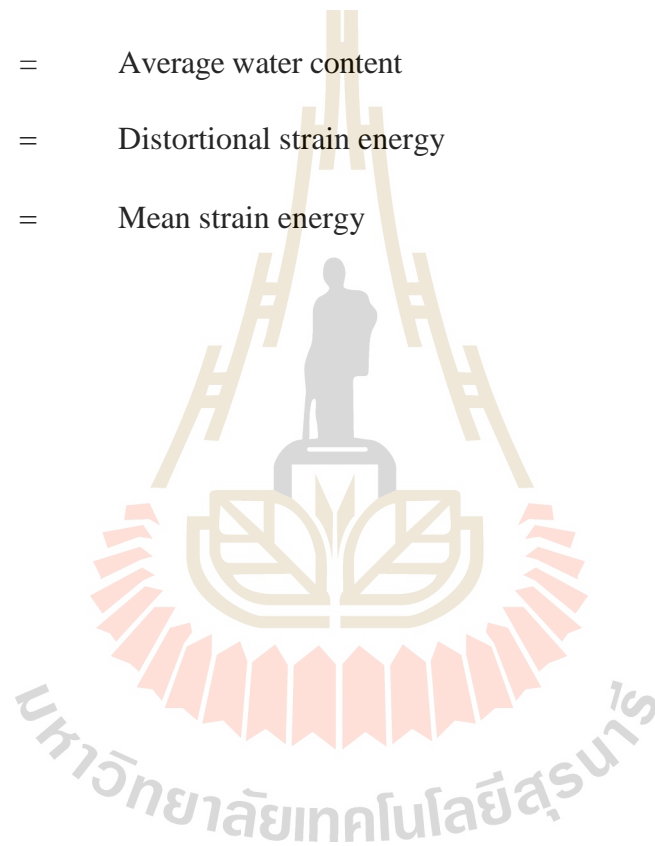
CHAPTER I

INTRODUCTION

1.1 Background and rationale

Water pressure is one of the most important factors influencing rock strength. It can decrease rock strength remarkably after only 1% water saturation (Vasarhelyi and Van, 2006; Dyke and Dobereiner, 1991). Understanding the nature behavior of rock mass is needed in geotechnical applications. The performance of engineering structures constructed in rock mass is concerned with the presence of fractures in rock when subjected to forces and displacements (Curran and Leong, 1983; Li et al., 2012). Rock masses properties, such as roughness, separation, water pressure and joint aperture have considerable effects on shear strength of rock fracture. The shear behavior is usually estimated through direct shear tests (e.g., ASTM D5607-08) to determine the peak and residual shear strengths of the rock fractures. The triaxial shear testing (Brady and Brown, 2006; Jaeger et al., 2007) has also been developed to simulate the frictional resistance of rock fractures under confinements. The normal stress at which the shear strengths are measured can be controlled by the applied axial stress and confining pressure. The effects of water pressure in rock fracture have long been recognized (Trimmer et al., 1980). The percent of water can reduce the rock mass strength (Torok and Vasarhelyi, 2010). The shearing resistance of fractures in saturated rock wall has however rarely been investigated.

1.2   Research objectives

The objective of this study is to determine the effects of pore pressure in fracture wall under confinement. The effort involves performing triaxial shear tests on tension-induced fractures and smooth saw-cut surfaces by using a polyaxial load frame. The fractures are sheared under various velocities. Phra Wihan sandstone is used as rock specimen.

1.3   Scope and limitations

The scope and limitations of the research include as follows.

1. All specimens are prepared from Phra Wihan sandstone.

2. The applied axial displacement rates vary from 10^{-5}, 10^{-4}, 10^{-3} to 10^{-2} mm/s with the confining pressures varying from 1, 3, 7, 12 to 18 MPa.

3. All tests are performed using a polyaxial load frame.

4. The fractures are artificially made in the laboratory by tension-inducing and saw-cut methods.

5. The nominal dimensions of $50 \times 50 \times 87$ mm^3 with the nominal fracture areas of 50×100 mm^2 are used.

1.4   Research methodology

This research methodology (Figure 1.1) comprises 7 steps, literature review, sample collection and preparation, sample Saturation, triaxial shear tests, empirical criterion, discussions and conclusions and thesis writing

1.4.1 Literature review

Literature review is carried out on experimental researches relevant to the effects of pore pressure, confining pressure and shear velocity on shear strength of sandstone. The sources of information are from text books, journals, technical reports and conference papers. A summary of the literature review is given in chapter two.
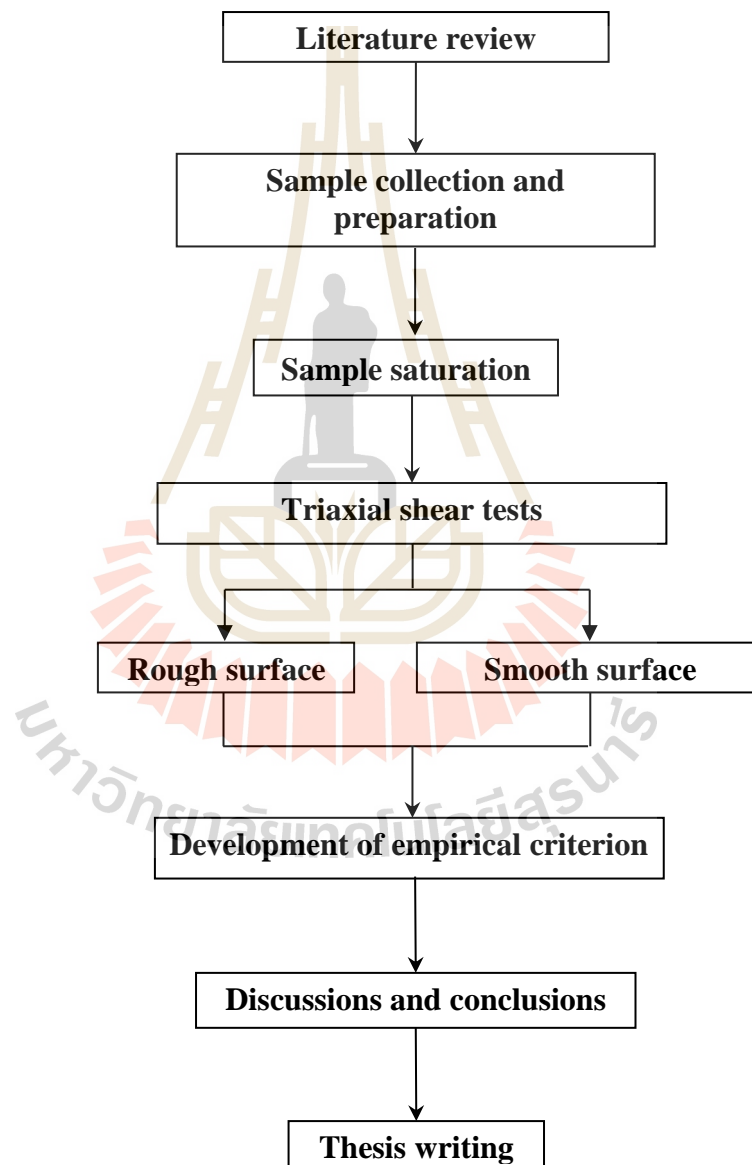
Figure 1.1 Research methodology.

1.4.2 Sample collection and preparation

The rock samples in this study are from Phra Wihan sandstone (Boonsener and Sonpiron, 1997) which has been prepared to obtain rectangular block specimens with nominal dimensions of $50\times50\times87$ mm^3 and shear surface with an area of 50×100 mm^2. The normal to the shear surface makes an angle 60° with the axis of the specimens.

- The rough surface is obtained by applying line load to diagonally across on rock specimens

- The smooth surface is obtained by using a saw cut to diagonally across on rock specimens.

1.4.3   Sample saturation

The sample is under saturated condition. They are submerged in a pressure vacuum chamber at a negative pressure of 0.1 MPa. Weights are measured every two hours. This pressure treatment is repeated until the weight remained unchanged.

1.4.4   Triaxial shear tests

Triaxial shear tests are performed to determine the peak shear strengths of tension-induced fractures and smooth surfaces under saturated condition. The normal to the fracture plane makes an angle of 60º with the axial (major principal) stress. The test uses a polyaxial load frame (Fuenkajorn and Kenkhunthod, 2010) is used to apply constant and uniform lateral stresses and vertical stress to the block specimen.

1.4.5 Development of empirical criterion

Results from laboratory study in terms of major principal stresses (σ_1) corresponding to the peak shear strength as a function of shear displacement (d_s), peak shear strength (τ) as a function of normal stress (σ_n) and peak shear strength (τ) as a function of shearing velocity ($\dot{d}_s$) for various confining pressures and under water saturated condition. The testing results have been used to develop relations between basic friction angle (ϕ_b), normal stress (σ_n), joint roughness coefficients (JRC) and shear stress (τ) for deriving a new failure criterion that can incorporate effect of shear velocity and water pressure on joint shear strength under confinements.

1.4.6 Discussions, conclusion and thesis writing

Empirical criterion is proposed to represent the fracture shear strengths as a function of normal stress and shear velocities.

1.5 Thesis contents

This research thesis is divided into six chapters. The first chapter includes background and rationale, research objectives, scope and limitations and research methodology. **Chapter II** presents results of the literature review to improve an understanding of the effects of pore pressure, confining pressure and shear velocity on shear strength of sandstone. **Chapter III** describes sample preparation. **Chapter IV** describes the laboratory testing. **Chapter V** presents analysis method. **Chapter VI** presents discussions, conclusions and recommendation for future studies.

CHAPTER II

LITERATURE REVIEW

2.1 Introduction

Relevant topics and previous research results are reviewed to improve an understanding the effects of pore pressure on mechanical properties of rock. These include the effects of pore pressure or water content on the shear strengths, cohesion and friction angle of rocks. The effects of loading rate and confining pressure on rock shear strength. Initial review results are summarized below.

2.2 Joint shear strength criteria

Patton (1966) proposes bilinear failure criterion, which offer a more realistic representation of the shear stress that can be developed along clean (unfilled) discontinuities. These criteria divide a typical curved envelope into two linear segments. The maximum shear strength that can be developed at failure is approximated by the following equations:

$$\tau_f = \sigma_n \tan (\phi_u + i) \tag{2.1}$$

where, τ_f is maximum (peak) shear strength at failure, σ_n is normal stress to the shear plane (discontinuity), ϕ_u is the basic friction angle on smooth planar sliding surface, and i is angle of inclination of the first order (major) asperities.

Barton and Choubey (1977) propose an empirical non-linear equation for peak shear strength of rough unfilled joints based on the results of direct shear tests performed on a wide variety of model tension fractures. The proposed equation for peak shear strength is as follows, which is sensitive both to variable joint roughness and compressive strength for the rock or joint walls:

$$\tau = \sigma_n \tan [JRC \log_{10}(\sigma_c/\sigma_n) + \phi_b] \tag{2.2}$$

where, τ is shear strength, σ_n is normal stress to the shear plane (discontinuity), σ_c is uniaxial compressive strength, ϕ_b is the basic friction angle on smooth planar sliding surface and JRC the Joint Roughness Coefficient.

Grasselli and Egger (2003) propose a new constitutive criterion, relating stress and displacements, is proposed to model the shear resistance of joints under constant normal load conditions. It is based on an empirical description of the surface, and on the results from more than 50 constant normal-load direct-shear tests performed on replicas of tensile joints and on induced tensile fractures for seven rock types. This constitutive model is able to describe experimental shear tests conducted in the laboratory. Moreover, the parameters required in the model can be easily measured through standard laboratory tests. The proposed criterion was also used to estimate the joint roughness coefficient (JRC) value. The predicting values were successfully correlated with JRC values obtained by back analysis of shear tests. Hence there is a need to develop an automated largescale direct shear testing machine to study the shear behavior of the jointed rock under CNL and CNS boundary conditions.

The machine must have the capability to study the influence of boundary conditions, shearing rate and infill on the shear behavior of rock joint.

Jaeger et al. (2007) state that in order to derive the laws that govern the transformation of stress components under a rotation of the coordinate system, one should consider a small triangular element of rock, as shown in Figure 2.1. The following equations are obtained for the normal and shear stresses acting on a plane whose outward unit normal vector is rotated counter clockwise from the x direction by an angle θ:

$$\sigma = \tfrac{1}{2}\,(\tau_{xx} + \tau_{yy}) + \tfrac{1}{2}\,(\tau_{xx} - \tau_{yy})\cos 2\,\theta + \tau_{xy}\sin 2\,\theta \tag{2.3}$$

$$\tau = \tfrac{1}{2}\,(\tau_{yy} - \tau_{xx})\sin 2\,\theta + \tau_{xy}\cos 2\,\theta \tag{2.4}$$

An interesting question to pose is whether or not there are planes on which the shear stress vanishes, and where the stress therefore has purely a normal component. The answer follows directly from setting τ = 0, and solving for:

$$\tan 2\,\theta = 2\tau_{xy}/\,(\tau_{yy} - \tau_{xx}) \tag{2.5}$$

A simple graphical construction popularized can be used to represent the state of stress at a point. Recall that equations (3) and (4) give expressions for the normal stress and shear stress acting on a plane whose unit normal direction is rotated from the x direction by a counterclockwise angle θ. Imagine that the principal coordinate system is used, in which the shear stresses are zero and the normal stresses are the two principal normal

stresses. In this case we replace τ_{xx} with σ_1, replace τ_{yy} with σ_2, replace τ_{xy} with 0, and interpret θ as the angle of counterclockwise rotation from the direction of the maximum principal stress. The following equations give the normal and shear stresses on a plane whose outward unit normal vector is rotated by θ from the first principal direction:

$$\sigma = \tfrac{1}{2}(\sigma_1 + \sigma_2) + \tfrac{1}{2}(\sigma_1 - \sigma_2)\cos 2\beta \tag{2.6}$$

$$\tau = \tfrac{1}{2}(\sigma_1 - \sigma_2)\sin 2\theta \tag{2.7}$$

The rock has a pre-existing plane of weakness whose outward unit normal vector makes an angle β with the direction of the maximum principal stress, σ_1 (Figure 2.2). The Coulomb criterion for slippage to occur along this plane is assumed to be:

$$|\tau| = S_0 + \eta\sigma \tag{2.8}$$

where σ is the normal traction component acting along this plane, τ is the shear component, S_0 is called the cohesion of the surface, and μ the coefficient of friction.
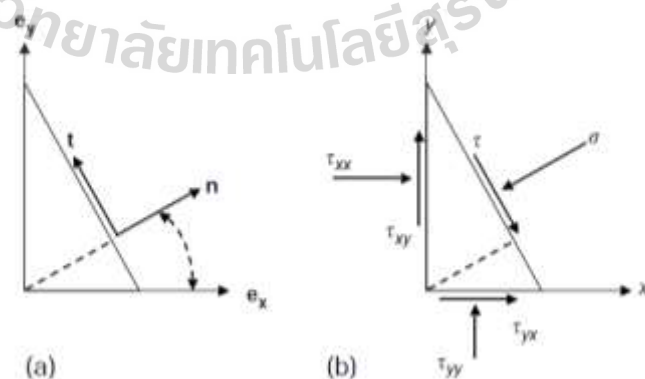
Figure 2.1 Small triangular slab of rock used to derive stress transformation equations (Jaeger et al., 2007).
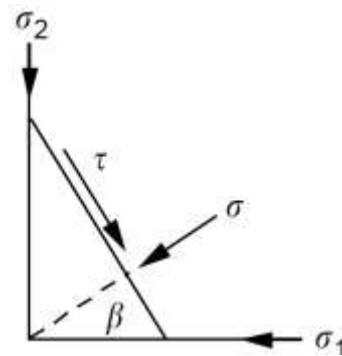
Figure 2.2 Plane of weakness with outward normal vector oriented at angle β to the
direction of maximum principal stress (Jaeger et al., 2007).

Shrivastava and Rao (2009) propose that for non-planar joint where the dilation
of the joint is resisted by surrounding rock mass, Constant Normal Stiffness (CNS) is a
proper boundary condition to investigate the shear behavior of joint than the Constant
Normal Load (CNL) boundary condition and CNS boundary condition will result in
higher shear strength. The effect of infill material and its thickness is to reduce the
shear strength of the rock joint. Shear rate, influences significantly the shear behavior
of rock joint. For shear behavior of joint under CNL boundary condition in the past
several researchers have attempted to explain the shear strength of rock discontinuities
under CNL boundary conditions. Linear failure criteria provided by Mohr-Coulomb.

$$\tau_f = c_a + \sigma_n \tan \phi_r \tag{2.9}$$

where τ_f is maximum (peak) shear strength at failure, σ_n is normal stress to the shear
plane (discontinuity), c_a is the apparent cohesion (shear strength intercept) derived from
the asperities and ϕ_r is the residual friction angle of the material comprising the
asperities.

2.3 Joint shear strength testing

Obert et al. (1976) study intact, induced-fractured and sawed samples of granite and sandstone. Tests were performed under variable constant normal stiffness (CNS). The results provided are somewhat limited however, with only detailed shear stress versus normal displacement results for two tests and peak shear versus peak normal stress for all tests.

Lee et al. (2001) study the mechanical behavior of rock masses, more specifically, joint properties such as roughness, strength of asperities, separation, gouge and even the spatial distributions make the behavior of jointed rock masses more complicated. Rock blocks sample of Hwangdeung granite and Yeosan marble, distributed in the southern part of Korea, were prepared with the dimension of sample size of up to length×width×height=$160 \times 120 \times 120$mm^3. Most of the previous laboratory experiments for the mechanical properties of rock joints have been focused on determining the peak shear strength and the stress–displacement relations under unidirectional shear loading. The comprehensive behavior of rock joints under the cyclic loading condition where the direction of shear load is repeatedly reversed has been rarely reported.

Morris (2003) states that the shear behavior of rock discontinuities is critical for understanding mechanical behavior of rock mass, because the shear movement of rock mass occurs mainly along the discontinuities such as faults, joints and fissures. Direct shear tests on the rock discontinuities can be divided into two types (Figure 2.3).
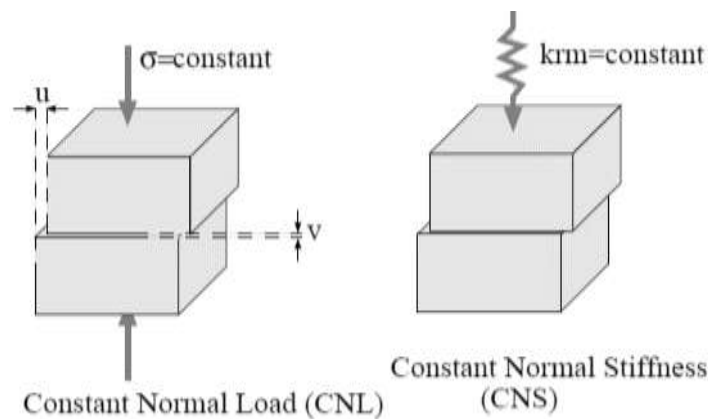
Figure 2.3 Constant Normal Load (CNL) and Constant Normal Stiffness (CNS) joint

shear tests (Morris, 2003).

- Constant Normal Load (CNL): The joint is confined by a constant normal

stress (σ_n) to the joint and measurements are conducted under increasing shear stress.

Even if the joint dilates, the apparatus serves to maintain a constant normal load on the

joint.

- Constant Normal Stiffness (CNS): The joint is confined by apparatus with

prescribed stiffness (krm). If the joint has tendency to dilate the normal stress (σ_n) will

increase as the surrounding apparatus responds. Typical the joint is subjected to an

initial normal stress (σ_{n0}).

Jiang et al. (2004) present a new direct shear apparatus for rock joints is

developed in order to accommodate the change in normal stress with dilation under the

CNS boundary condition. A rational experimental procedure is described for the

determination of the shear behavior of rock joints. The normal stiffness can be set

automatically (Figure 2.4) according to the deformational capacity of the surrounding

rock masses. Shear tests on artificial joint specimens are carried out using the newly
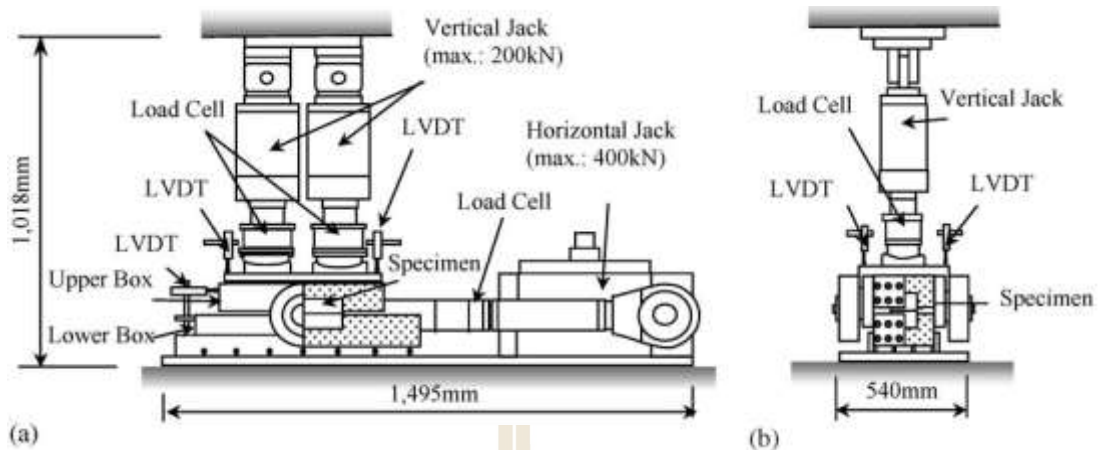
Figure 2.4 Digital-controlled shear testing apparatus: (a) side view and (b) front view

(Jiang et al., 2004).

developed apparatus in order to clarify the influence of the boundary conditions (i.e. constant normal load and constant normal stiffness) on the shear behavior of rock joints

Kapang et al. (2013) perform the true triaxial shear tests and direct shear tests have been performed to determine the peak shear strengths of tension-induced fractures and smooth surfaces in three Thai sandstones Phu Kradung, Phu Phan and Phra Wihan sandstones (hereafter designated as PKSS, PPSS and PWSS) to the $76 \times 76 \times 126$ mm^3 rectangular block specimens. The normal to the fracture plane makes an angle of 59.1° with the axial (major principal) stress. The experiment was divided into 4 parts as follows:

(1) true triaxial shear tests of tension-induced fractures under constant σ_p/σ_o ratio.

(2) True triaxial shear tests of tension-induced fractures under constant σ_p,.

(3) True triaxial shear tests of smooth surfaces under constant σ_p.

(4) Direct shear tests of tension-induced fractures.

Results of this study it can be concluded that the lateral stress (σ_p) parallel to the sliding plane and perpendicular to the sliding direction can significantly reduce the cohesion and friction angle of the fractures. The greater magnitudes of the lateral stress σ_p result in larger sheared off areas and larger dilations. In general the decrease of the fracture cohesion with increasing confining pressures (for the case of lateral stress ratio $\sigma_p/\sigma_o =$ 1) as observed here agrees reasonably well with the experimental results obtained by Ramamurthy and Arora (1994). This means that the fracture shear strengths from the (unconfined) direct shear testing may not rock asperities into the fracture gap. These asperities can be sheared off more easily when the fractures are subject to shear load, and hence resulting in a lower frictional resistance. This is evidenced by the fact that σ_p has no effect on the shear strength of smooth saw-cut surfaces. The reduction of the cohesion and friction angle probably depends on the roughness characteristics (amplitudes, scale, and asperity strength). Fractures in other rocks, that have different surface roughness and strengths from those tested here, may exhibit different degrees of the σ_p-dependency. Different shear strength criteria may be required to describe the results if the τ-σ_n relationship is non-linear. The proposed relation is supported by the fact that the test results from the direct shear testing and from the true triaxial shear testing under $\sigma_p = 0$ are very similar. More testing is required on various rock types and fracture characteristics to further investigate the effects of fracture roughness, scale and strength of the asperities (e.g. Fardin et al., 2001), and incorporate them into the proposed polyaxial shear strength criterion.

2.4   Effects of pore pressure on rock

Hawkins and McConnell (1992) determine the influence of the water content on the strength of 35 sandstones (Figure 2.5). They found that the relationship between water content and uniaxial compressive strength could be described by an exponential equation of the form:

$$\sigma_c(w) = ae^{-bw + c} \tag{2.10}$$

where σ_c (w) is the uniaxial compressive strength (MPa), w is the water content (%) and a, b and c are constants. It is obvious that the strength at zero water $\sigma_{c0} = a + c$, the strength at full saturation $\sigma_{csat} = c$. The parameter b is a dimension less constant defining the rate of strength loss with increasing water content.
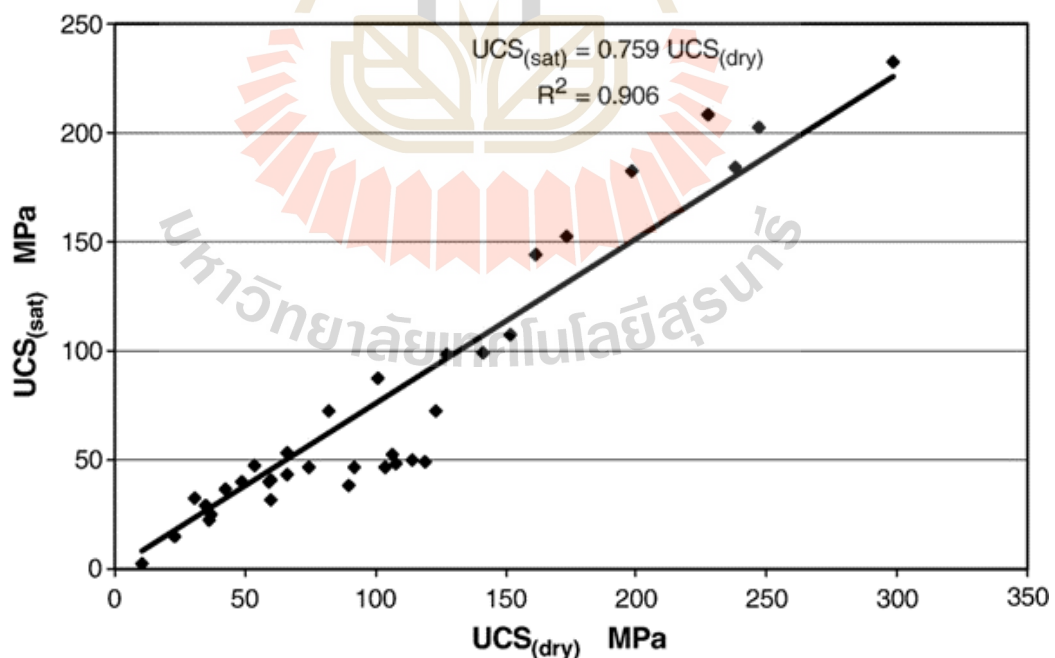
Figure 2.5 Relationship between dry and saturated uniaxial compressive strength (UCS) for 35 British sandstones (Hawkins and McConnell, 1992).

Vasarhelyi (2003) determines the unconfined compressive strength (UCS), the tangent and secant Young's modulus of 35 British sandstones tested in the dry and saturated states. Although the 35 British sandstones have different mineral contents, porosity, grain size, etc. The data for UCS and tangent/secant Young's modulus given by Hawkins and McConnell (1992) have been analyzed and a linear regression established between the petrophysical constants of the dry and saturated materials. The high R^2 values show that there is a distinct relationship between the dry and saturated properties. Statistically the saturated UCS is 75.6% of the dry (Figure 2.6), While the saturated tangent and secant moduli are 76.1 and 79.0% of the dry samples respectively (Figure 2.7). The slopes of the lines are close to each other thus it can be assumed that the influence of the degree of saturation is the same for the different petrophysical constants. The relationship between these constants was also examined. In every case, the slopes of the lines were independent of the water content. These values were around 176 and 147 for the UCS/tangent and UCS/secant moduli respectively and about 0.82 for the E_{tan}/E_{sec} relationship (Figures 2.8 and 2.9).
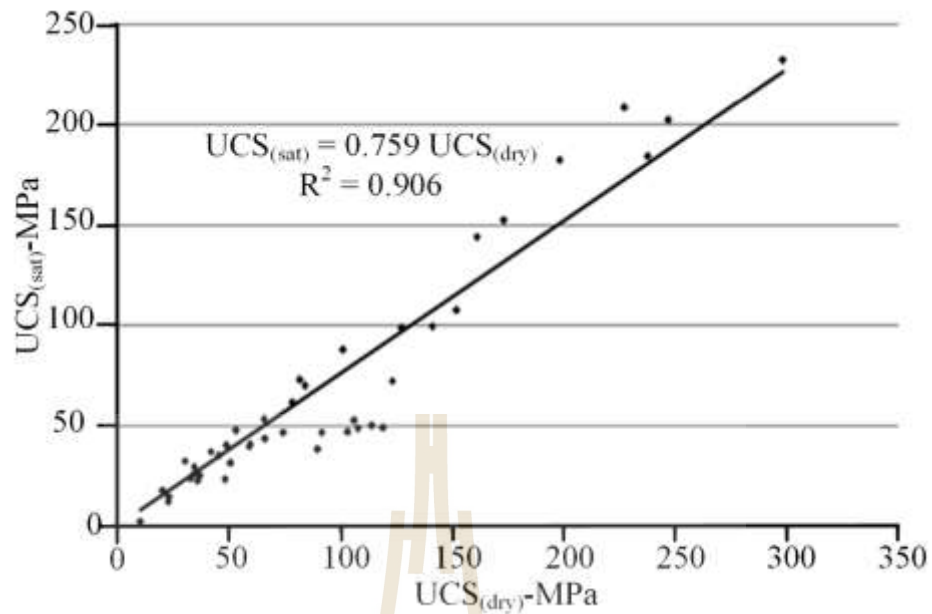
Figure 2.6 Relationships between dry and saturated UCS for 35 British sandstones (Vasarhelyi, 2003).
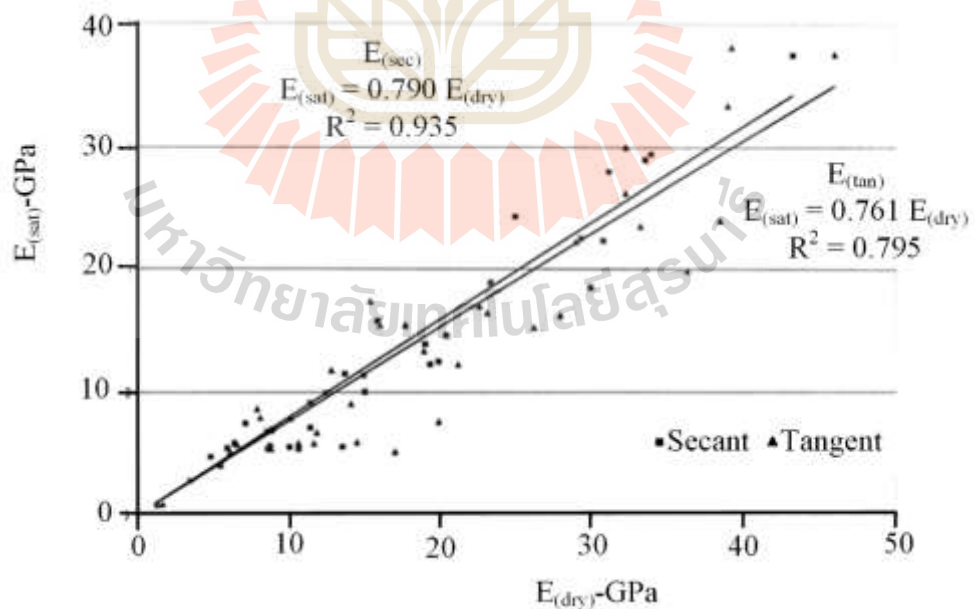
Figure 2.7 Relationships between dry and saturated Young's modulus for 35 British sandstones (Vasarhelyi, 2003).
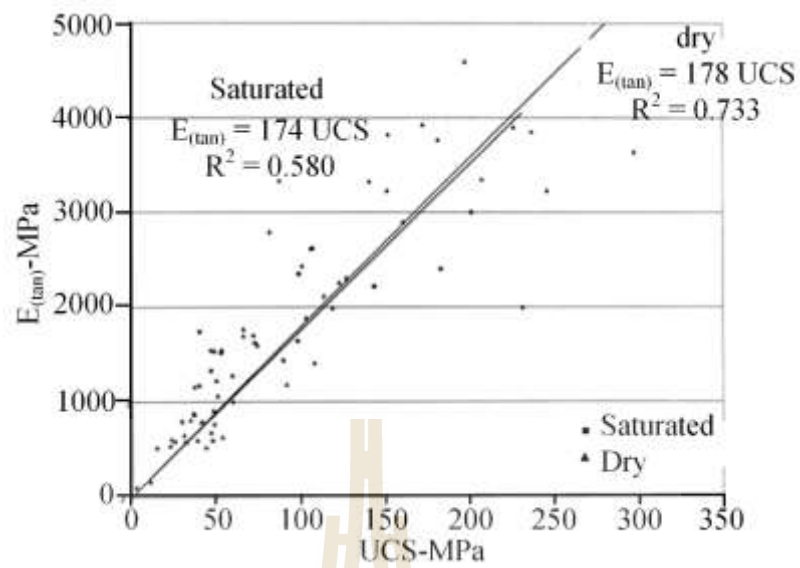
Figure 2.8 Relationships between the unconfined compressive strength (UCS) and the

tangent Young's modulus (E_{tan}) in dry and saturated conditions (Vasarhelyi,
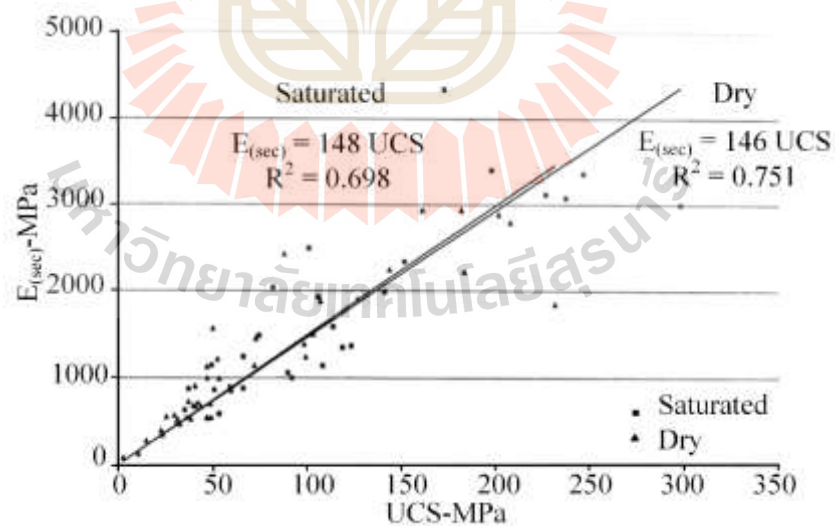
2003).

Figure 2.9 Relationships between the unconfined compressive strength (UCS) and the

secant Young's modulus (E_{sec}) in dry and saturated conditions (Vasarhelyi,

2003).

Vasarhelyi and Van (2006) study the rock strengths under dry and water saturated conditions to show a method for estimating the sensivity of sandstone rocks to water content. From an analysis results of Hawkins and McConnell (1992), they found that the relationship between water content and uniaxial compressive strength could be described by an exponential equation of the form:

$$\sigma_c(w) = a \cdot \exp(-bw + c) \tag{2.11}$$

Where σ_c (w) is the uniaxial compressive strength (MPa), w is the water content (%) and a, b and c are constants. Figure 2.10 shows the best-fit lines plotted for the 15 different rock types for water content values up to 5%. It is apparent that the strength of the rock is very sensitive to the water content an increase in water content of as little as 1% from the dry state can have a marked effect on strength. The disadvantage of the analysis method of Hawkins and McConnell (1992) is that the saturated condition differs for each of the investigated sandstone. Further, the suggested fitting curve of Equation (10) (Hawkins and McConnell, 1992) changes if the relative water content goes to infinity. For a better representation of the moisture dependence, they suggest a recalculation of the material constants a, c, b. With the water content expressed using an absolute measure such as the degree of saturated. This means that for all rock, S=0 in the case of dry conditions and S=1 in the case of fully conditions. However, they suggest a different form for the exponential function of Equation (11), considering that the fully saturated condition is achieved at 100% water content.
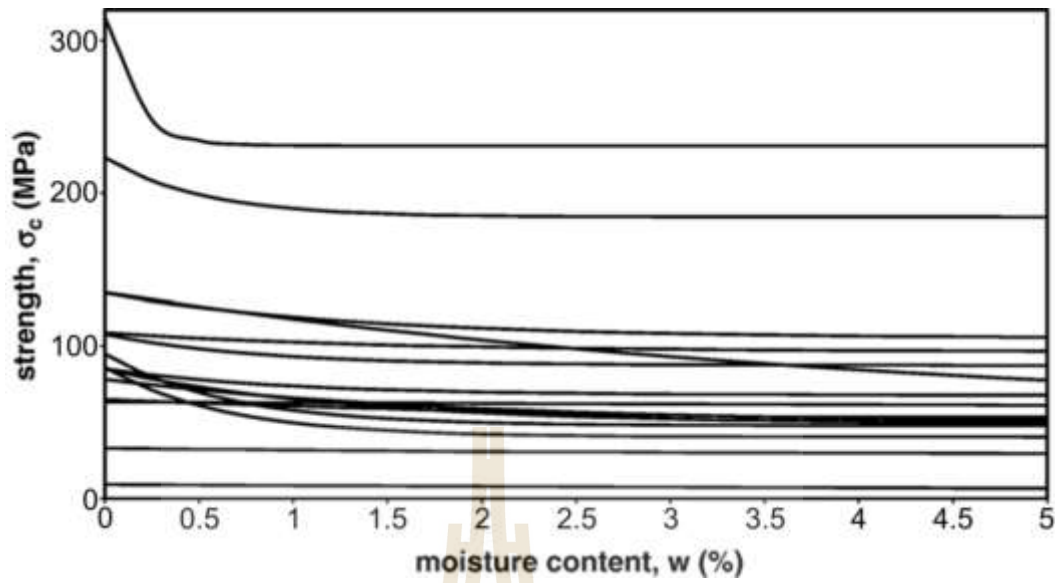
Figure 2.10 Relationship between strength (σ_c) as function of water content (w) of 15 different rock types for water content values up to 5% (Vasarhelyi and Van, 2006).

In the proposed expression, given by Equation (12), the exponential dependence is preserved.

$$\sigma_c(w) = a^* + c^* e^{-b^*w} \tag{2.12}$$

$$a^* = \sigma_{co} - ((\sigma_{co} - \sigma_{csat})/1 - e^{-b^*}) \tag{2.13}$$

$$b^* = -\ln(0.1/(\sigma_{co} - \sigma_{csat})) \tag{2.14}$$

$$c^* = (\sigma_{co} - \sigma_{csat})/(1 - e^{-b^*}) \tag{2.15}$$

The strength-water content curve recalculated using the proposed expressions (Equation (12)) are presented at Figure 2.11. An advantage of the presented method is

that less tests are necessary for calculating the influence of the water content on the rock properties. From measurements of the density and the uniaxial compressive strength in case of dry and saturated petrophysical states. The strength as a function of water content can be easily determined, both in terms of relative (i.e. water content as a percentage of the rock mass) and absolute (i.e. degree of saturation) scales.

Yilmaz (2010) studies the influence of water content on the unconfined strength and elastic modulus of gypsum rock samples tested under dry and saturated conditions. UCS and E_t versus water content graphs (Figure 2.12) indicated that even a very small increase in water content (1-2) % causes a considerable loss in the strength of gypsum. The results show that the UCS and E_t of gypsum have been reduced by water immersion and that the strength of gypsum is very sensitive to water content. The relationships between dry and saturated parameters were analyzed using correlations between UCS_{dry} − UCS_{sat}, $E_{t,dry}$ − $E_{t,sat}$ (Figure 2.13)
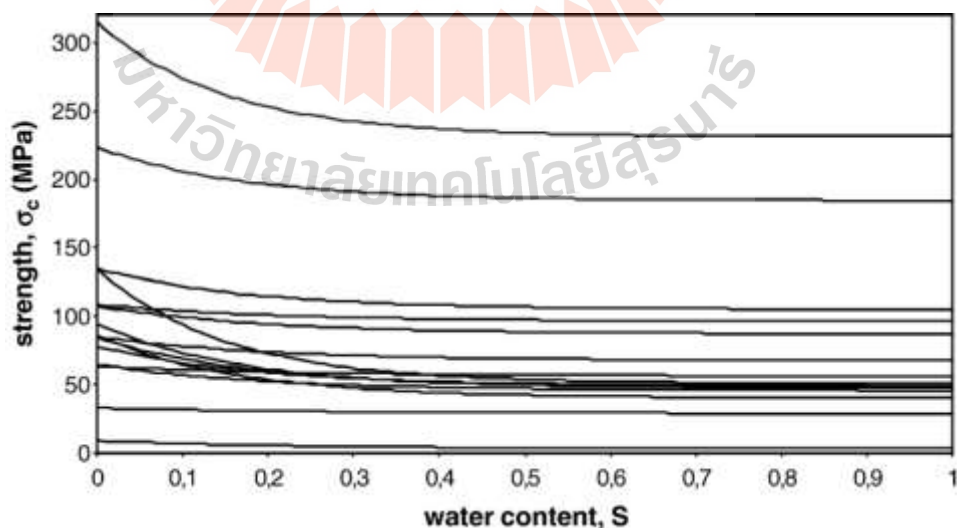
Figure 2.11 Relationships between strength (σ_c) as function of water content (Vasarhelyi and Van, 2006).
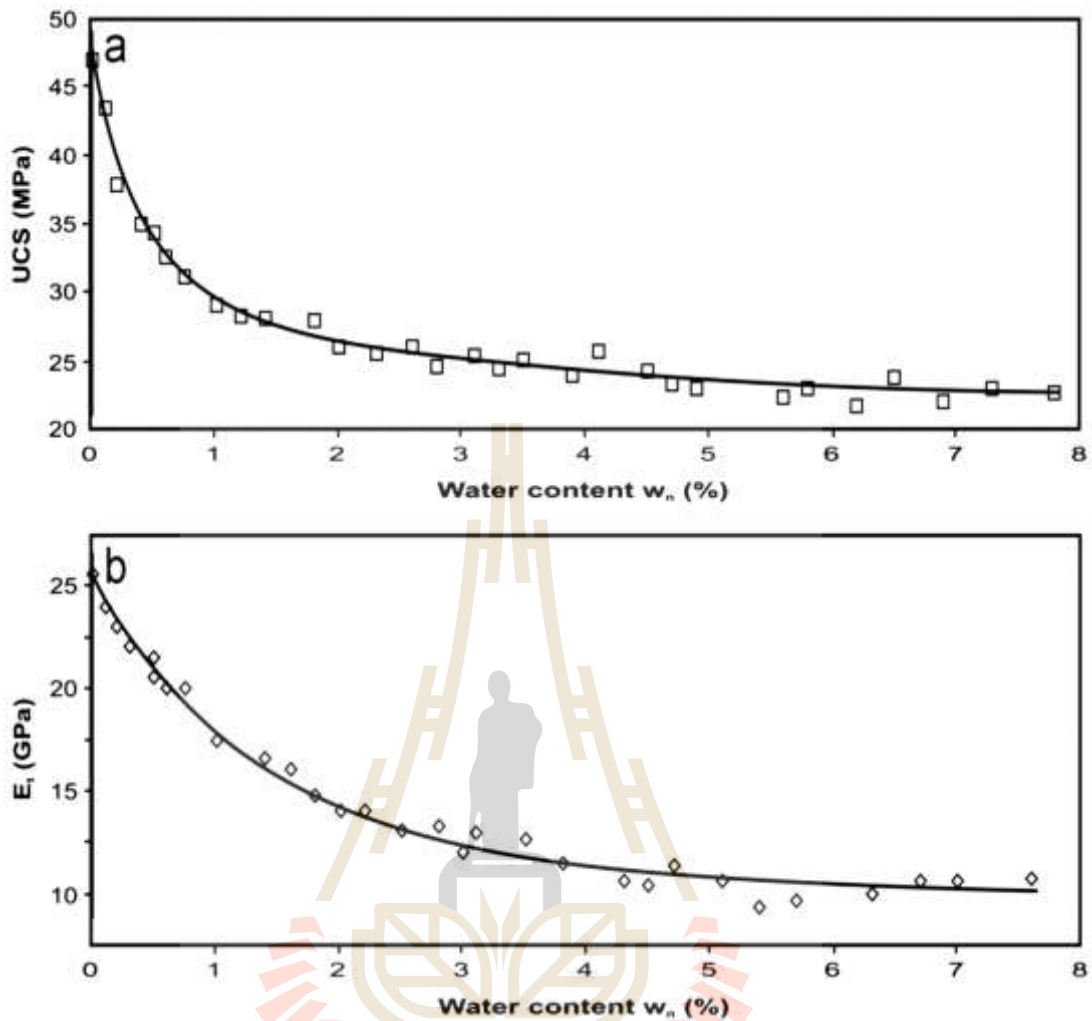
Figure 2.12 Curves of water content versus unconfined compressive strength (a) and elasticity modulus (b) (Yilmaz, 2010).

and relationships derived as expressed by empirical equations of $UCS_{sat} = 0.3492UCS_{dry}$ and $E_{t,sat} = 0.5363E_{t,dry}$. Test results revealed that as the water content increased from dried to saturated condition, the values of UCS and E_t decreased as much as, 64.07 and 53.05%, respectively. Saturated gypsum reached failure at relatively low stress compared to dry gypsum
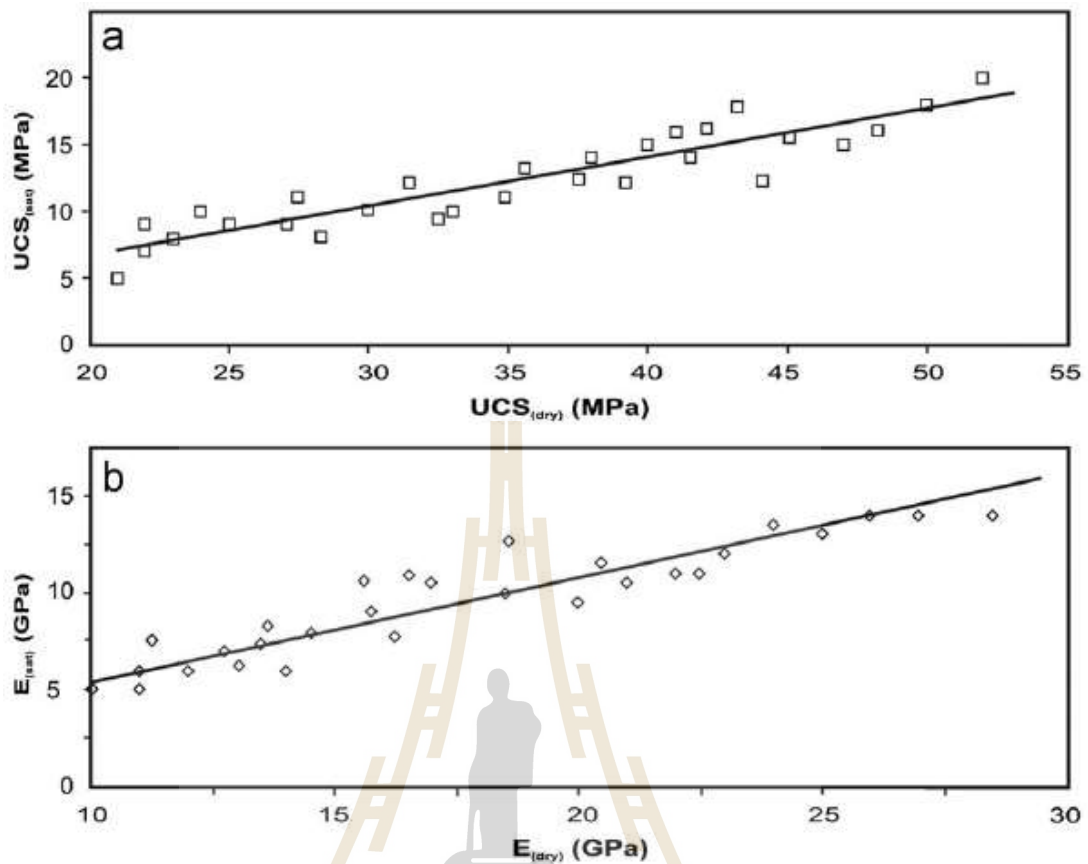
Figure 2.13 Relationships between dry and saturated unconfined compressive strength

(a) and elasticity modulus (b) of gypsum samples (Yilmaz, 2010).

Khamrat et al. (2016) study the influence of water content under triaxial compressive strength testing in 6 rock type are granite, marl, marble Phu Phan sandstone, Phra Wihan sandstone, and Phu Kradung siltstone under loading rates ($\partial\sigma_1/\partial t$) of 0.001 MPa/s, 0.1 MPa/s, and 1 MPa/s. Testing is made under both dry and wet conditions. Under dry condition the specimens were dried in an oven for 24 h before testing. To wet the rock specimens, they were submerged in water in a pressure vacuum chamber at a negative pressure of 0.1 MPa. The physical properties of rock specimens are shown in Table 2.1. Rock specimens under high loading rate and high confining a strength higher than those

under low loading rate and low confining both dry and wet conditions are presented at Figure 2.14. The strength of the dry specimens was always greater than that of the wet one, as has been found for Denizli travertinel, homogeneous Indian granite, sandstone, and limestone. The differences in strengths between the wet and dry specimens increased with confining pressures. The rock specimens with higher porosity (Phra Wihan sandstone) yielded larger strength difference than those with lower porosity (granite, marl, marble, Phu Phan and Phu Kradung sandstones).

2.5 Effect of shear velocity

Li et al. (1999) study the effects of strain rate on rock material properties under triaxial compression on the Bukit Timah granite of Singapore. A sample were tested at four strain rates (10^{-4} to 10^{-1}) and 6 confining pressures (20, 50, 80, 110, 140 and 170 MPa). The test results show that the compressive strength generally increases with increasing strain rate and confining pressure, as shown in Figures 2.15 and 2.16.

Table 2.1 Physical properties of rock specimens (Khamrat et al., 2016).

Rock Types	Dry density (g/cm^3)	Wet density (g/cm^3)	Water content w (%)	Effective porosity η (%)
Granite	2.64 ± 0.04	2.65 ± 0.06	0.14 ± 0.03	0.37 ± 0.06
Marl	2.49 ± 0.05	2.55 ± 0.05	2.71 ± 0.62	6.70 ± 1.40
Marble	2.74 ± 0.04	2.74 ± 0.04	0.09 ± 0.03	0.26 ± 0.07
PP Sandstone	2.42 ± 0.05	2.47 ± 0.04	2.05 ± 0.22	4.97 ± 0.51
PW Sandstone	2.25 ± 0.06	2.36 ± 0.04	4.91 ± 0.38	11.00 ± 0.97
PK Sandstone	2.53 ± 0.03	2.57 ± 0.02	1.53 ± 0.38	3.88 ± 0.98
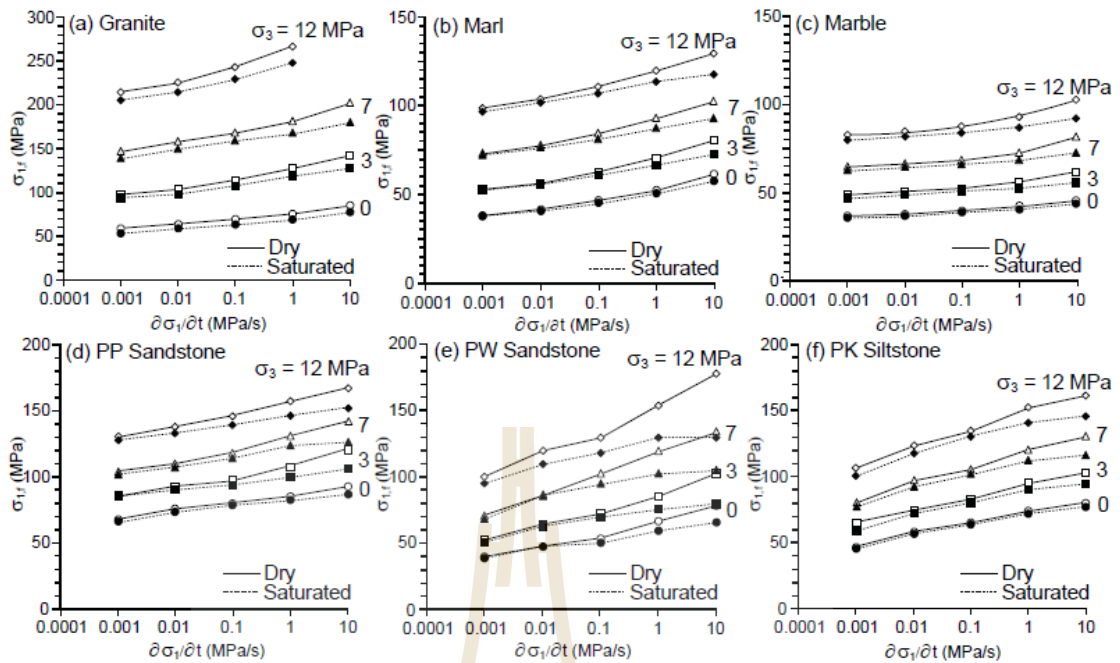
Figure 2.14 Major principal stress ($\sigma_{1,f}$) as a function of loading rate ($\partial\sigma_1/\partial\sigma_t$.). (Khamrat et al., 2016).

The rate of increment of compressive strength with strain rate is lower at higher confining pressure. The results for the Young's modulus and the Poisson's ratio at different strain rates and confining pressure are scattered. The Young's modulus seems to increase slightly with increasing confining pressure, but appears to be unaffected by strain rate. The Poisson's ratio seems to increase slightly with increasing strain rate and confining pressure. Further tests are needed to overcome the scattering of the results and to obtain conclusive indications on the possible changes of the Young's modulus and the Poisson's ratio.

Ray et al. (1999) study the effect of cyclic loading and strain rate on the mechanical behavior of sandstone. The results indicate that the percentage decrease in

uniaxial compressive strength was found to increase with the increase in applied stress level and direct proportionality between the two parameters was found. The uniaxial compressive strength of Chunar sandstone was determined at strain rates of 2.5×10^1/s, 2.5×10^0 and 2.5×10^{-1}/s and found to be 99.5 MPa, 75.1 MPa and 64.0 MPa, respectively. A clear increase in uniaxial compressive strength was, therefore, observed with increase strain rate. The failure strength was found to increase with the increase of strain rate and an abrupt increase in strength was noticed at the strain rate of 2.5×10^1/s. Stress was found to increase with the increase in strain rate (Figure 2.17) and Young's modulus was found to increase with the increase in strain rate (Figure 2.18).
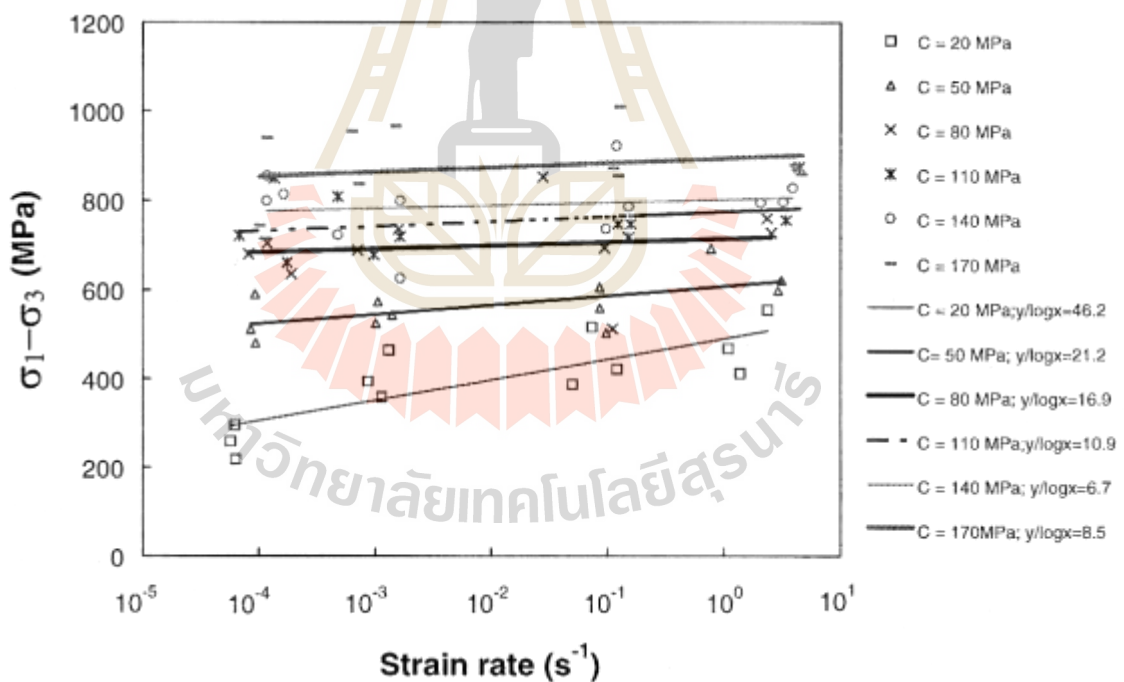
Figure 2.15 Variation of the compressive strength with the strain rate at different confining pressure (Li et al., 1999).
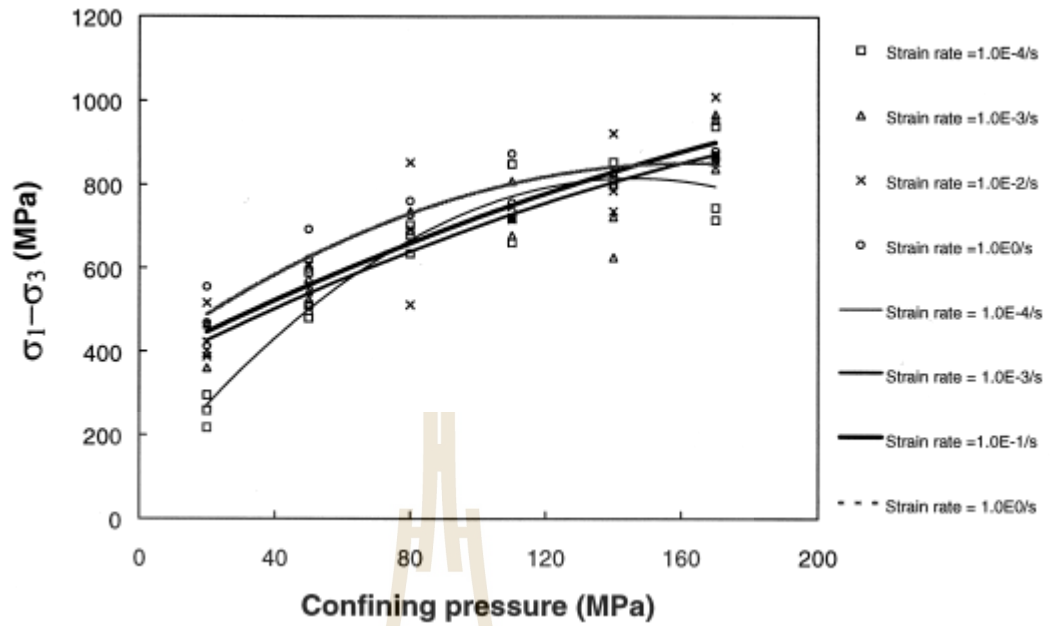
Figure 2.16 Variation of the compressive strength with the confining pressure at different strain rates (Li et al., 1999).
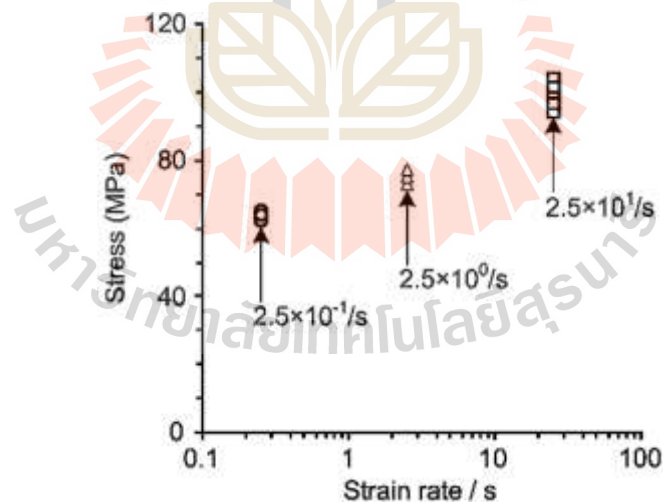
Figure 2.17 Stress as function of strain rate (Ray et al., 1999).
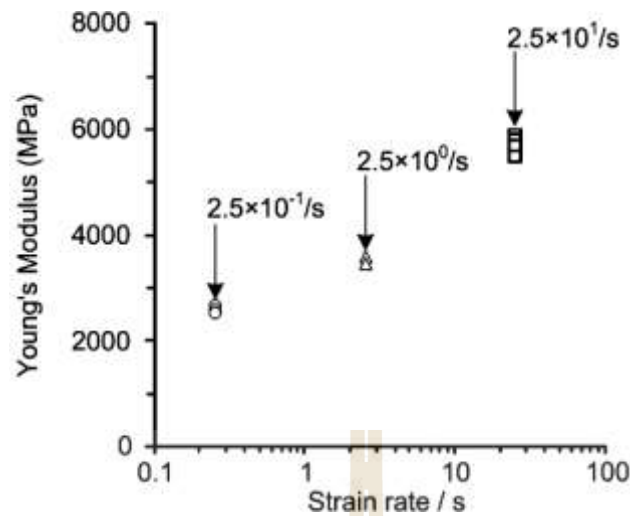
Figure 2.18 Young's modulus as function of strain rate (Ray et al., 1999).

Fuenkajorn and Kenkhunthod, (2010) study the influence of loading rate on deformability and compressive strength of three Thai sandstones. Uniaxial and triaxial compressive strength tests have been performed using a polyaxial load frame to assess the influence of loading rate on the strength and deformability of three Thai sandstones. The applied axial stresses are controlled at constant rates of 0.001, 0.01, 0.1, 1.0 and 10 MPa/s. The confining pressures are maintained constant at 0, 3, 7 and 12 MPa. The sandstone strengths and elastic moduli tend to increase exponentially with the loading rates. The average Poisson's ratios are 0.36, 0.38 and 0.15 for the PP, PW and PK sandstones, respectively. Under the confining pressure of 12 MPa extension fractures dominate. The stress-strain curves obtained from the triaxial loading tests under various loading rates for the three sandstones are plotted in Figure 2.19. An empirical loading rate dependent formulation of both deformability and shear strength is developed for the elastic and isotropic rocks. It is based on the assumption of constant distortional strain energy of the rock at failure under a given mean normal stress.

The proposed multiaxial criterion well describes the sandstone strengths within the range of the loading rates used here. It seems reasonable that the derived loading rate dependent equations for deformability and shear strength are transferable to similar brittle isotropic intact rocks.
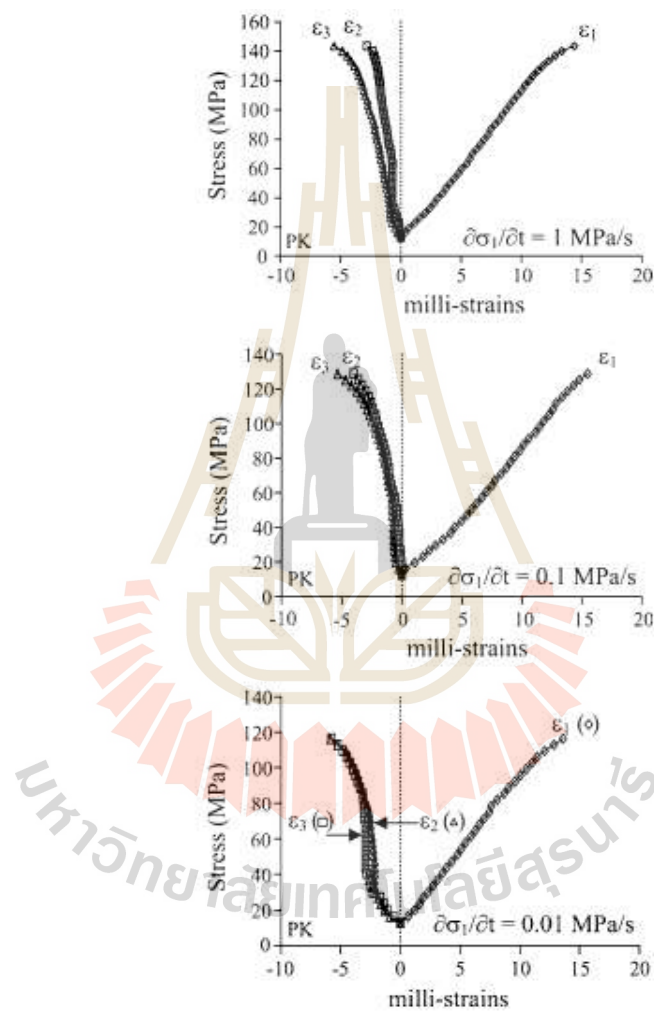
Figure 2.19 Examples of triaxial compressive strengths for PK sandstone with axial loading rates of 1, 0.1, and 0.01 MPa/s under the confining pressure of 12 MPa (Fuenkajorn and Kenkhunthod, 2010).

Kleepmek et al. (2016) performed triaxial shear tests to assess the effects of displacement velocity and confining pressure on shear strengths and dilations of tension-induced fractures and smooth saw-cut surfaces prepared in granite, sandstone and marl specimens. The specimens are prepared to obtain rectangular blocks with nominal dimensions of $50 \times 50 \times 87$ mm^3. They have nominal areas of 50×100 mm^2. Confining pressures between 1 and 18 MPa with displacement velocities ranging from 1.15×10^{-5} to 1.15×10^{-2} mm/s. Under each confining stress (σ_3), the differences between the peak and residual stresses notably reduced when the fractures are subjected to lower shear velocities. These differences tend to be smaller for fractures with lower JRC values (marl and sandstone) as compared to those with higher JRC values (granite). The major principal stresses, shear strengths and dilation rates of rough fractures for the peak and residual increase with displacement velocities and the result of shearing resistances on smooth saw-cut surfaces tend to be independent of the displacement velocity and confining pressure. Figure 2.20 show major principal stresses increase with increasing displacement velocities in same confining pressure.

Granite

Sandstone

Marl
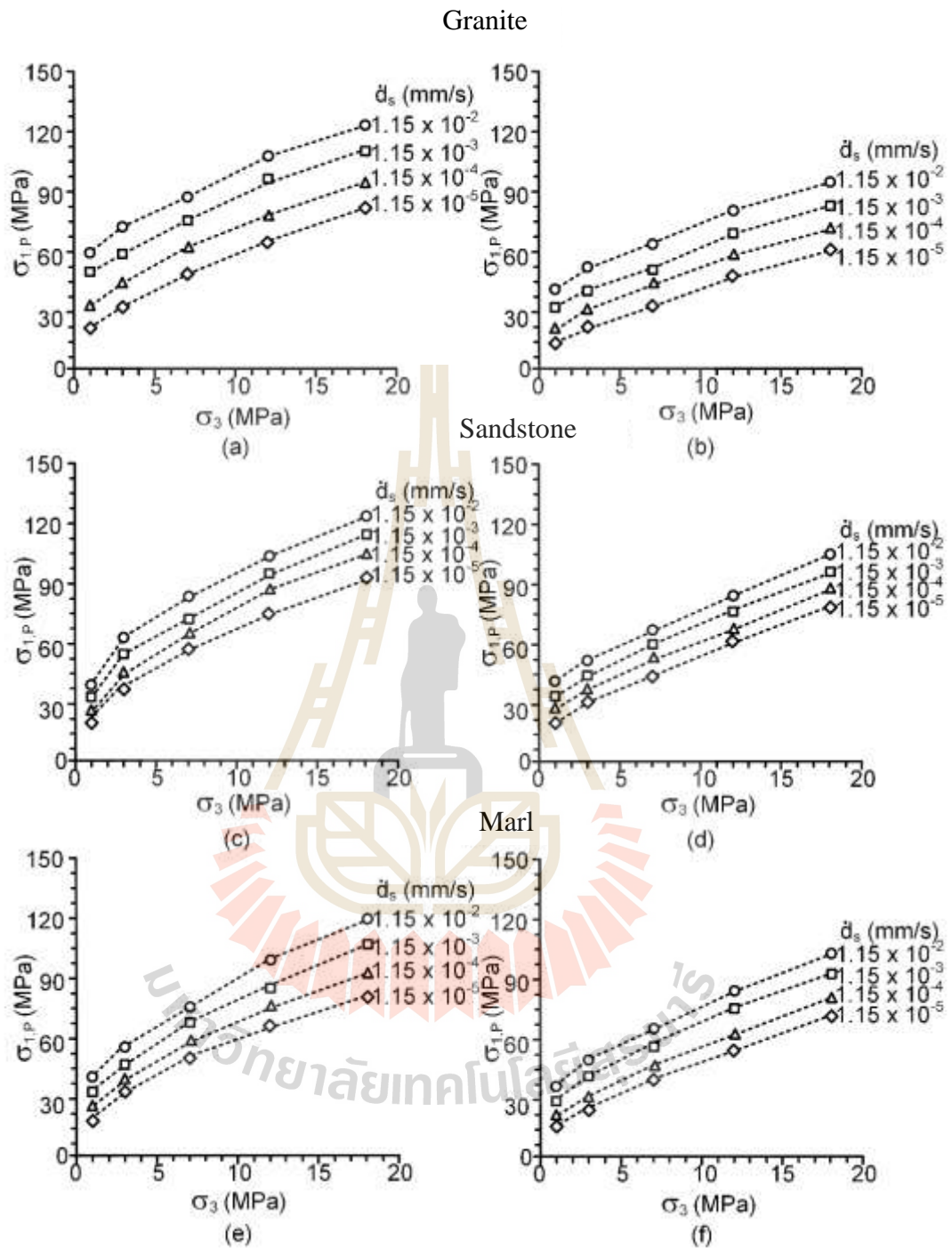
Figure 2.20 Major principal stresses at peak, $\sigma_{1,P}$ (a, c, e) and at residual, $\sigma_{1,R}$ (b, d, f) as a function of confining stresses (σ_3) (Kleepmek et al., 2016).

CHAPTER III

SAMPLE PREPARATION

3.1 Introduction

This chapter describes the sample preparation for the triaxial shear testing on tension-induced fractures and smooth saw-cut surfaces. The rock samples used in this study are Phra Wihan sandstone. Khamrat et al. (2016) give the descriptions of the rock. The mechanical properties of the tested rocks obtained from related studies are given in Table 3.1

Table 3.1 Mechanical properties of Phra Wihan sandstone.

Properties	Values	Sources
Elastic modulus (GPa)	10.8	Fuenkajorn and Kenkhunthod, (2010)
Cohesions (MPa)	3.1	Kapang et al. (2013)
Friction angles (degrees)	46.0	Kapang et al. (2013)
Biaxial extension strength (MPa)	15.0	Phueakphum et al. (2013)
Tensile strengths (MPa)	6.7	Phueakphum et al. (2013)
Biaxial flexural tensile strength (MPa)	6.6	Phueakphum et al. (2013)
Uniaxial compressive strength under dry condition (MPa)	54.0	Khamrat et al. (2016)
Uniaxial compressive strength under saturated condition (MPa)	51.0	Khamrat et al. (2016)
Cohesions form triaxial test under dry condition (MPa)	11.2	Khamrat et al. (2016)
Friction angles form Triaxial under dry condition (degrees)	47.0	Khamrat et al. (2016)
Basic friction angles (degrees)	33.5	Kleepmek et al. (2016)

3.2 Sample preparation

The sandstone is prepared to obtain rectangular block specimens with nominal dimensions of $50 \times 50 \times 87$ mm^3. The fractures have nominal areas of 50×100 mm^2, as shown in Figure 3.1. The fractures are artificially made in the laboratory by tension inducing method (Figure 3.2) and smooth saw-cut surface made by using a universal masonry saw. The normal to the fracture plane for both tension-induced fracture and smooth saw-cut surface makes an angle 60° with the axis of the specimens. The maximum roughness amplitudes on the fracture planes are measured from the laser-scanned profiles (Figure. 3.3) which are used to determine the joint roughness coefficients (JRC) of each fracture based on the Barton's chart (Barton, 1982). The means and standard deviations of the JRC's are 10 ± 0.5. Figure 3.4 shows examples of the laser scanned profiles.
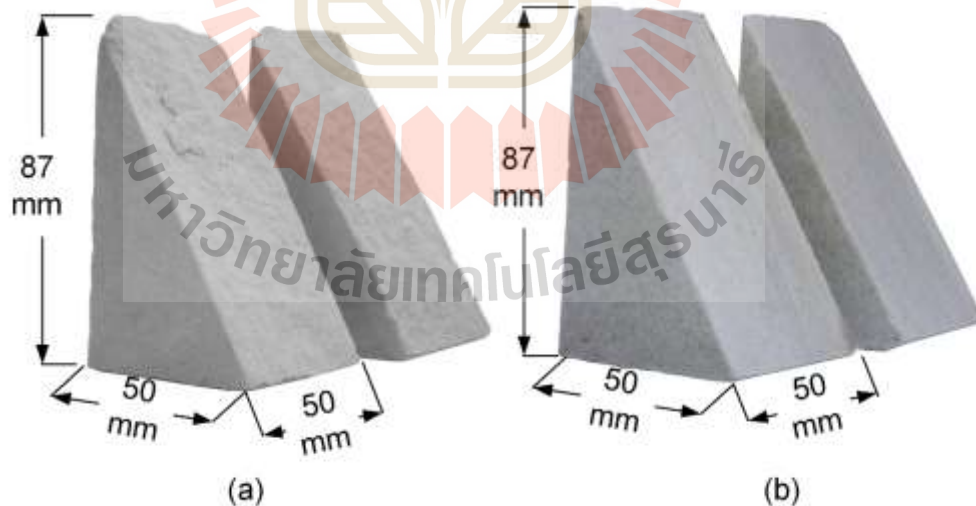
Figure 3.1 Some rectangular block specimens of Phra Wihan sandstone used in triaxial shear test on rough (a) and smooth fractures (b).
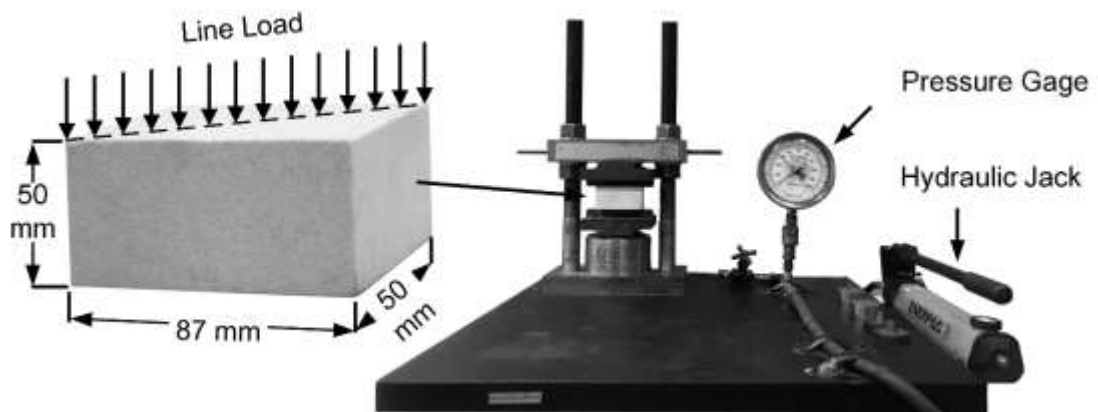
Figure 3.2 Tension-induced fracture by line loading technique.

3.3   Sample saturation

After fracture is made the specimens are tested under saturated condition. They are submerged in a pressure vacuum chamber at a negative pressure of 0.1 MPa (Figure 3.5). Their weights are measured every two hours. This pressure treatment are repeated until the weight remained unchanged. Figure 3.6 shows water contents as function of time. The average of water contents ($w_{ave.}$) from all specimens are 5.02%. Tables 3.2 and 3.3 show physical properties and dimensions of specimen before testing.
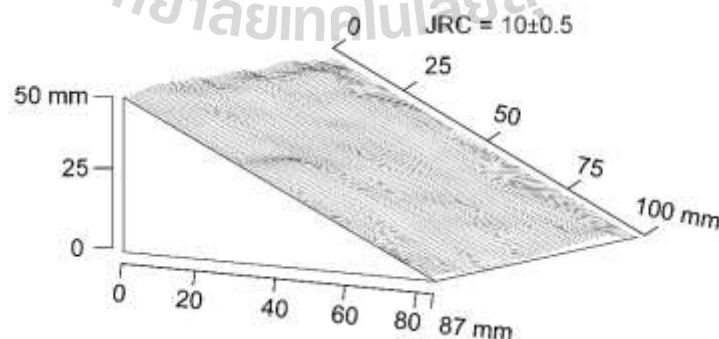
Figure 3.3 Example of laser scanned image of tension-induced fracture.
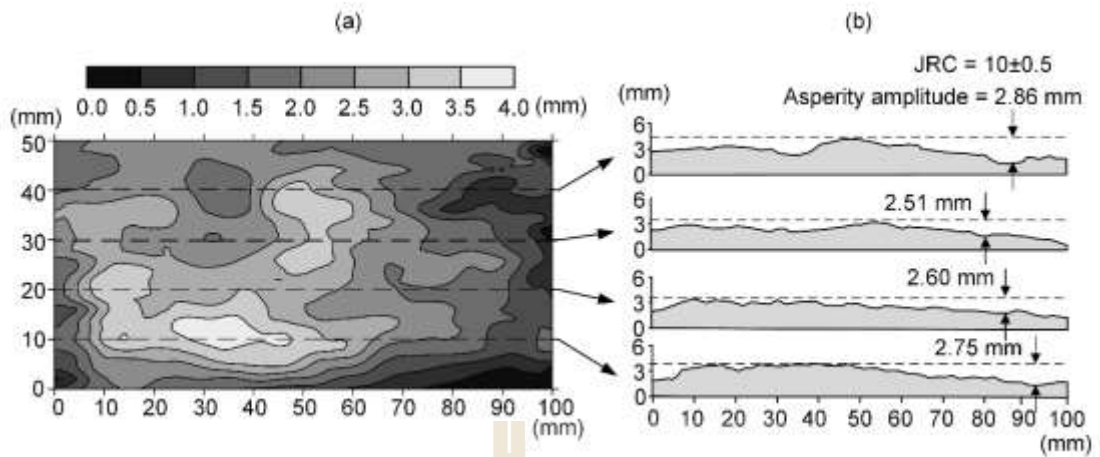
Figure 3.4 Examples of fracture contour (a) laser-scanned profiles (b) used to measure the maximum asperity amplitude to estimate the joint roughness coefficient (JRC).
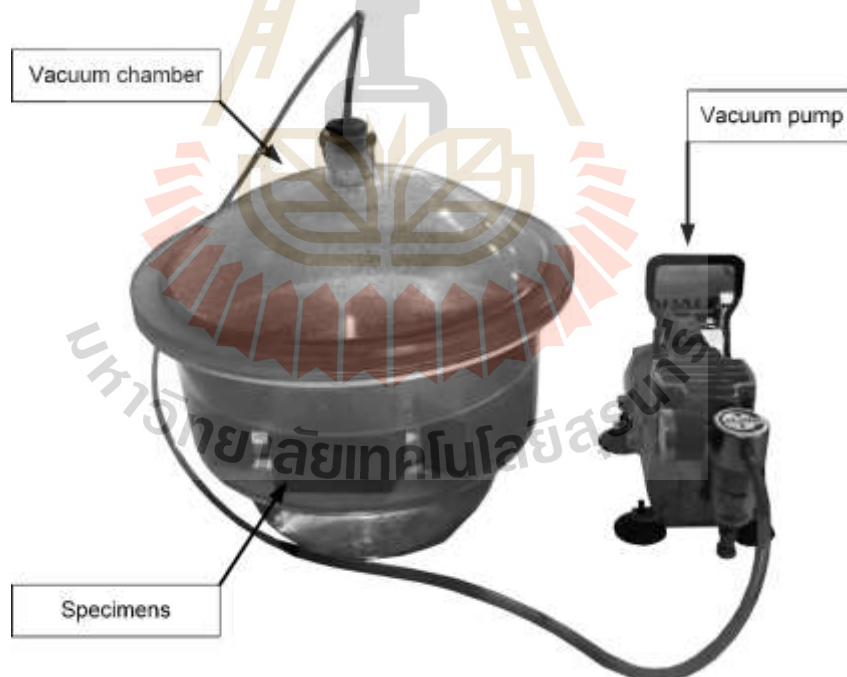
Figure 3.5 Rock specimens saturated under water in vacuum chamber.
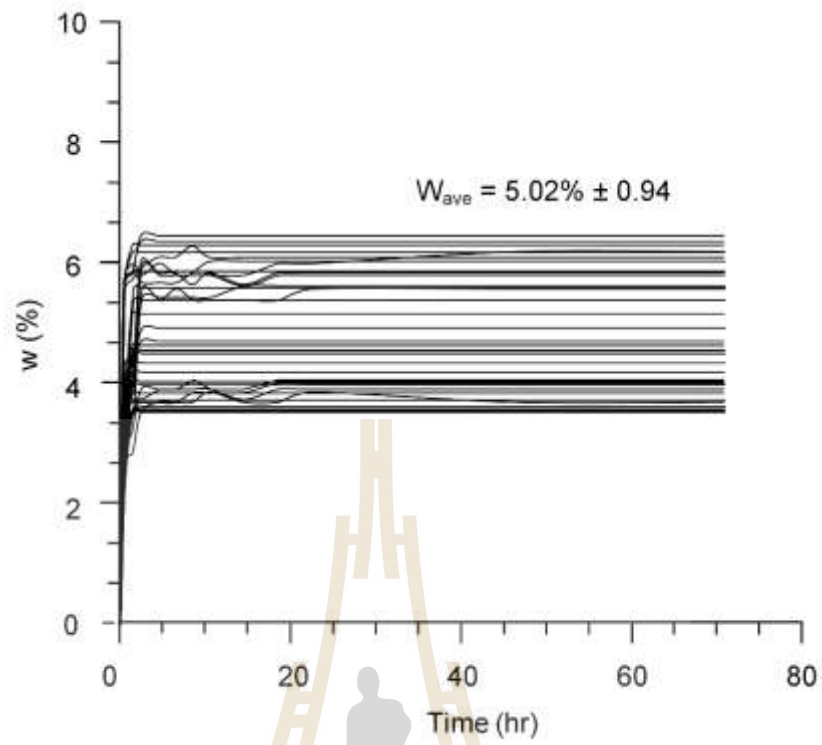
Figure 3.6 Water contents as function of time for all specimens.

Table 3.2 Summary physical properties and dimension of rough fracture specimens.

Sample No.	Dimensions (mm)	Dry Density (g/cc)	Sat. Density (g/cc)	Water Contents (%)
PW-01	51.80×51.34×87.63	2.23	2.32	4.06
PW-02	51.26×51.04×86.39	2.32	2.41	4.01
PW-03	49.22×49.51×87.81	2.23	2.37	6.10
PW-04	50.67×50.90×87.35	2.24	2.37	5.87
PW-05	49.05×48.83×87.20	2.24	2.38	6.18
PW-06	48.95×48.57×87.64	2.22	2.35	6.04
PW-07	51.00×51.13×87.10	2.17	2.27	4.73
PW-08	50.81×50.39×87.29	2.33	2.44	4.55
PW-09	51.28×51.16×87.23	2.38	2.49	4.66
PW-10	49.36×48.00×87.31	2.25	2.36	4.59
PW-11	50.95×51.11×87.98	2.35	2.43	3.13
PW-12	50.65×50.57×87.34	2.32	2.47	6.52
PW-13	51.01×50.98×86.60	2.37	2.50	5.79
PW-14	51.22×51.27×88.50	2.35	2.48	5.90
PW-15	51.35×51.22×87.80	2.22	2.32	4.71
PW-16	51.36×50.34×87.21	2.24	2.34	4.64
PW-17	51.24×51.36×87.64	2.32	2.41	3.91
PW-18	50.93×50.82×87.65	2.27	2.35	3.70
PW-19	49.25×49.05×87.86	2.25	2.38	5.83
PW-20	50.51×50.50×87.42	2.37	2.51	5.81
PW-21	50.85×50.93×87.71	2.36	2.49	5.59
PW-22	50.74×51.02×87.64	2.26	2.39	5.62
PW-23	50.50×50.81×87.28	2.35	2.44	3.51
PW-24	51.50×51.35×86.07	2.36	2.44	3.44
PW-25	51.13×51.59×87.50	2.22	2.31	4.35
PW-26	49.98×50.13×86.31	2.31	2.42	4.66
PW-27	48.64×48.91×86.66	2.27	2.40	5.97
PW-28	48.95×49.36×87.64	2.25	2.39	6.13
PW-29	51.04×51.17×87.21	2.34	2.52	7.38
PW-30	50.89×51.11×87.63	2.37	2.46	3.72
PW-31	51.35×50.80×87.40	2.25	2.33	3.50
PW-32	50.40×51.15×86.62	2.31	2.40	3.83
PW-33	49.08×48.98×87.21	2.22	2.33	5.17
PW-34	50.35×50.32×87.68	2.31	2.40	4.03
PW-35	50.31×49.95×87.48	2.34	2.44	4.57
PW-36	48.90×49.05×87.69	2.22	2.30	3.58
PW-37	51.32×51.30×87.83	2.24	2.37	5.58
PW-38	50.39×50.27×87.05	2.29	2.42	5.37
PW-39	50.93×51.05×87.20	2.34	2.47	5.78
PW-40	50.37×50.61×87.56	2.33	2.46	5.82

Table 3.3 Summary physical properties and dimension of smooth fracture specimens.

Sample No.	Dimensions (mm)	Dry Density (g/cc)	Sat. Density (g/cc)	Water Contents (%)
PW-01	52.24×52.31×87.22	2.31	2.43	4.88
PW-02	51.93×51.40×87.45	2.27	2.37	4.36
PW-03	50.18×51.08×86.94	2.25	2.36	4.85
PW-04	48.80×49.19×86.50	2.34	2.45	4.47
PW-05	51.51×51.65×87.57	2.37	2.48	4.51
PW-06	50.11×49.83×87.47	2.25	2.35	4.53
PW-07	50.44×51.21×87.78	2.31	2.42	4.44
PW-08	47.96×50.42×86.53	2.22	2.31	4.33
PW-09	49.45×51.07×88.15	2.31	2.41	4.62
PW-10	50.55×48.09×87.15	2.34	2.42	3.54
PW-11	50.47×49.94×87.73	2.22	2.31	4.18
PW-12	51.27×51.94×87.41	2.24	2.32	3.52
PW-13	48.00×50.95×86.55	2.29	2.40	4.51
PW-14	48.62×49.95×88.14	2.34	2.42	3.63
PW-15	50.77×51.27×87.26	2.33	2.46	5.92
PW-16	49.46×49.11×86.55	2.33	2.47	6.04
PW-17	50.78×50.80×86.13	2.31	2.45	6.04
PW-18	51.06×47.92×87.59	2.30	2.43	6.02
PW-19	51.45×48.49×87.34	2.34	2.49	6.24
PW-20	50.44×49.75×86.96	2.35	2.50	6.20

CHAPTER IV

LABORATORY TESTING

4.1   Introduction

The objective of the laboratory testing is to assess the effects of pore pressure on shear strength of fracture in rock under confining pressure. This chapter describes the method and results of the laboratory experiments.   There are two types of discontinuities: tension-induced fractures and smooth saw-cut surfaces. The results have been studied to determine the effects of pore pressure ,confining pressure and loading rate on triaxial shear strength of the fractures. The results obtained have are also compared with other researches.

4.2   Triaxial shear strength test

A polyaxial load frame (Fuenkajorn and Kenkhunthod, 2010) (Figure 4.1) is used to apply constant and uniform lateral stresses (confining pressures, $\sigma_2=\sigma_3$) and vertical stress or axial stress (σ_1) to the block specimen. Figure 4.2 shows the directions of the applied stresses with respect to fracture orientation. The confining pressures are maintained constant at 1, 3, 7, 12 and 18 MPa for tension-induced fractures, and at 3, 7 and 12 MPa for smooth saw-cut surfaces. The shear stress (τ) and its corresponding normal stress (σ_n) on the fracture can be determined from the applied principal stresses (σ_1 and σ_3) as follows (Jaeger et al., 2007; Barton, 2013):
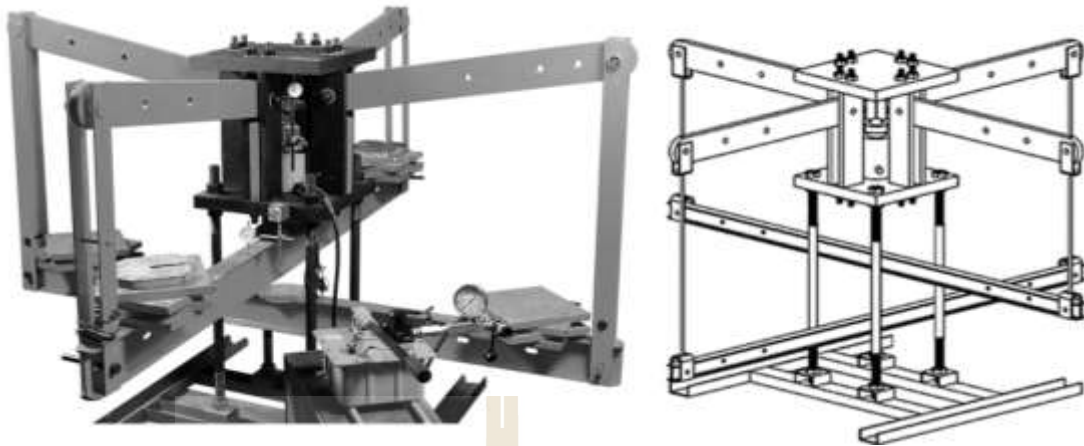
Figure 4.1 Polyaxial load frame (Fuenkajorn and Kenkhunthod, 2010).
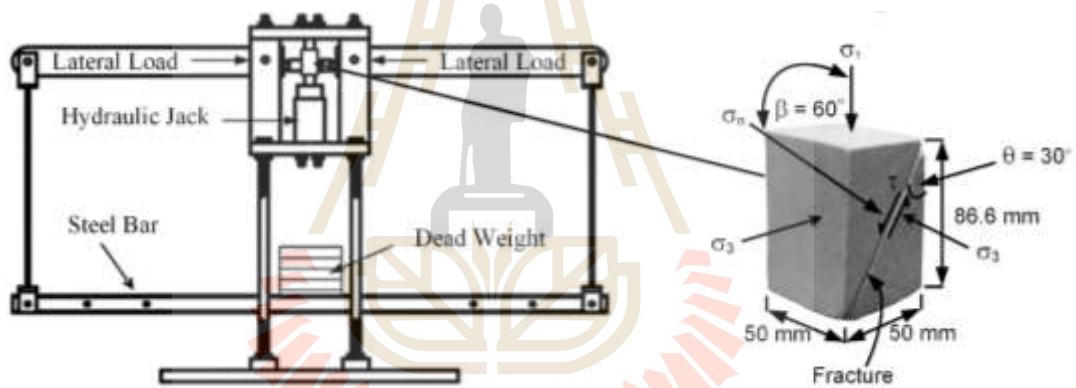
Figure 4.2 Directions of the applied stresses with respect to fracture orientation.

$$\tau = \frac{1}{2}(\sigma_1 - \sigma_3) \cdot \sin 2\beta \qquad (4.1)$$

$$\sigma_n = \frac{1}{2}(\sigma_1 + \sigma_3) + \frac{1}{2}(\sigma_1 - \sigma_3) \cdot \cos 2\beta \qquad (4.2)$$

where β is the angle between σ_1 and σ_n axis. The shear and normal (dilation) displacements (d_s and d_n) can also be calculated from the vertical and lateral displacements (d_1 and d_3) as:

$$d_s = d_1 / \sin \beta \tag{4.3}$$

$$d_n = (d_{3,m} - d_{3,c}) \cdot \sin \beta \tag{4.4}$$

$$d_{3,c} = \tan(90-\beta) \cdot d_1 \tag{4.5}$$

$$d_{3,m} = \text{Vertical movement of steel beam} / 12 \tag{4.6}$$

where $d_{3,m}$ is the total lateral displacement measured during the test, and $d_{3,c}$ are the calculated lateral displacement induced by the vertical displacement on the incline fracture plane. Using Eq. (4.3) the shear displacement velocities (d_s) that are equivalent to the applied axial displacement velocities ($\dot{d}_s$) of 10^{-5}, 10^{-4}, 10^{-3} and 10^{-2} mm/s are calculated as 1.15×10^{-5}, 1.15×10^{-4}, 1.15×10^{-3} and 1.15×10^{-2} mm/s. Figure. 4.3 shows the direction relations of the fracture displacements. Kleepmek et al. (2016) study the influence of frictional resistance at the interfaces between the loading platens and the lateral neoprene sheets are determined by vertically loading an intact specimen with the same dimensions while the constant lateral stresses parallel to the fracture applied. Results are shown in Figure. 4.4. After installing the rectangular specimen into the load frame, dead weights are placed on the steel bar to obtain the pre-defined magnitude of the uniform lateral stress (σ_2 and σ_3) on the specimen. The test is started by increasing the vertical stress or axial stress (σ_1) at the predefined rate using the hydraulic pump. Both the axial strain and lateral strain were properly recorded directly by a dial gage during the testing. The failure shear stresses are recorded and mode of failure examined.
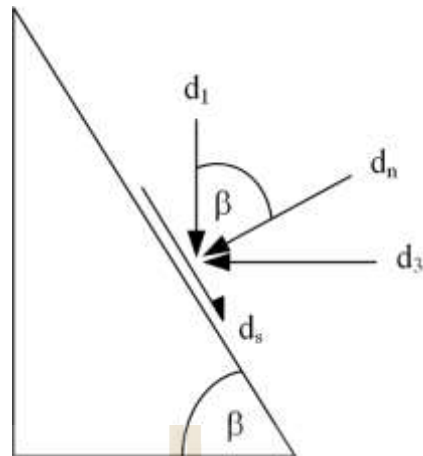
Figure. 4.3 Direction relations of the fracture displacements.
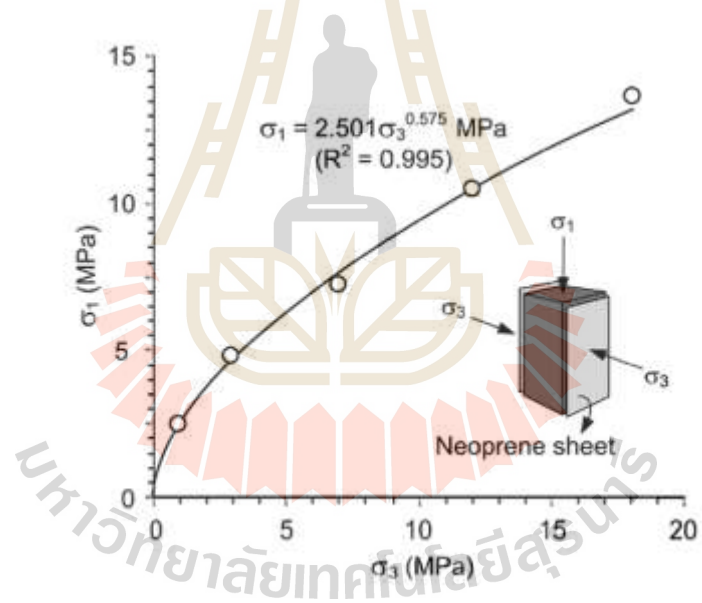
Figure. 4.4   Axial resistance between loading platens and neophrene sheets induced

by lateral stress (σ_3). (Kleepmek et al., 2016)

4.3   Test results on tension-induced fractures

The results are presented in forms of shear stress as a function of shear displacement, shear strengths at peak and residual regions as a function of normal stress, principal stress at peak and residual regions as a function of normal stress and dilation of the fractures during shearing. The shear stress-displacement (τ-d_s) curves obtained under all displacement velocities are shown in Figure 4.5. Under each confining stress (σ_3), the differences between the peak and residual stresses notably reduced when the fractures are subjected to lower shear velocities.

The shear stresses are plotted as a function of normal stresses in Figure 4.6 for both peak and residual. They have non-linear behavior. The effects of the shear velocity can be seen by the reduction of the shear stresses as the shear velocities decrease. The major principal stresses for the peak ($\sigma_{1,P}$) and residual ($\sigma_{1,R}$) increase with displacement velocities (Figure 4.7). The peak and residual shear strengths corresponding confining pressure are shown in the figure. The decreasing rate of the peak and residual stresses tend to be uniform with the changes of the order of the shear velocities.
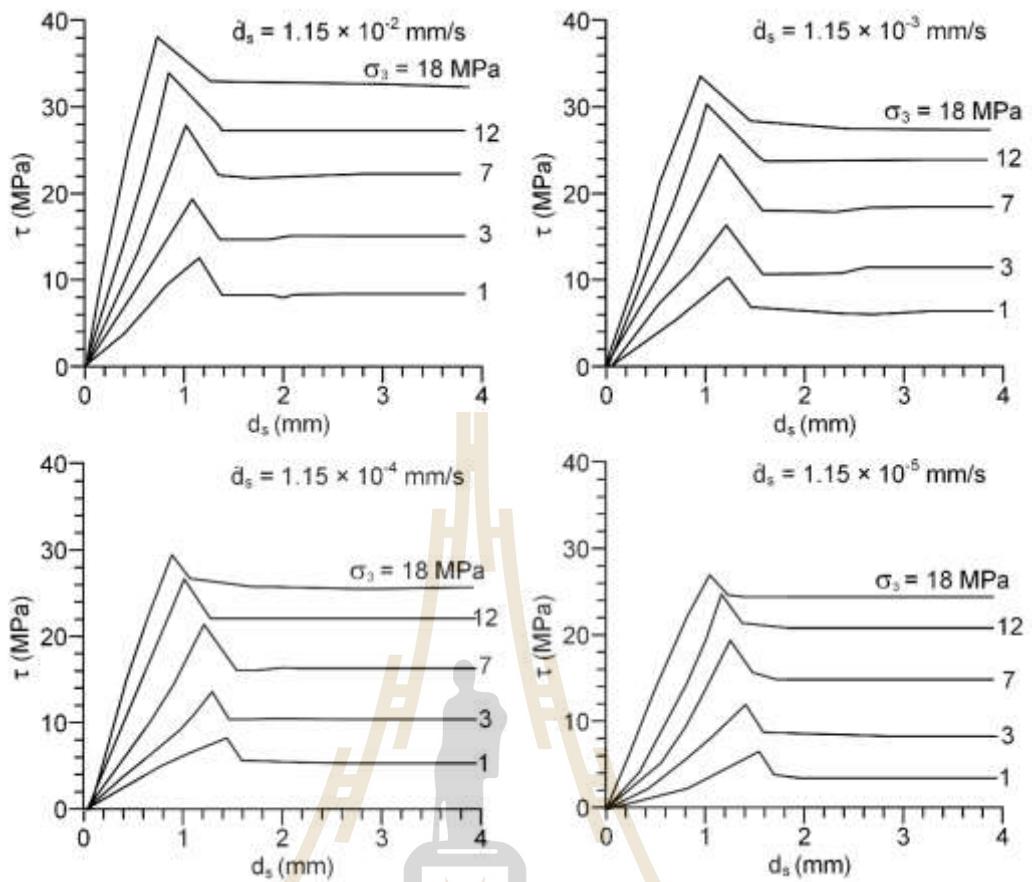
Figure. 4.5 Shear stresses (τ) as a function of shear displacement (d_s).
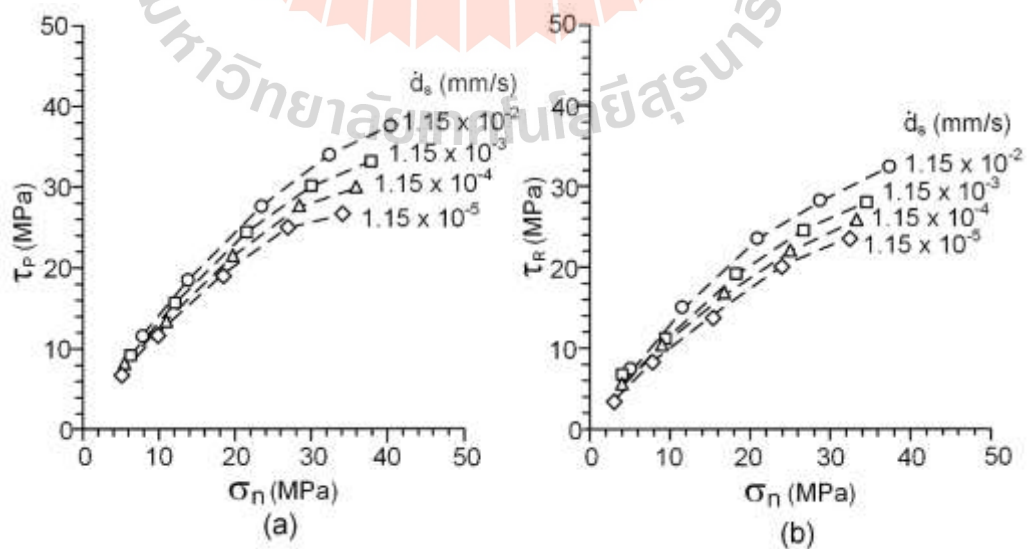
Figure. 4.6 Peak shear strengths (τ_p) as a function of normal stress (σ_n).
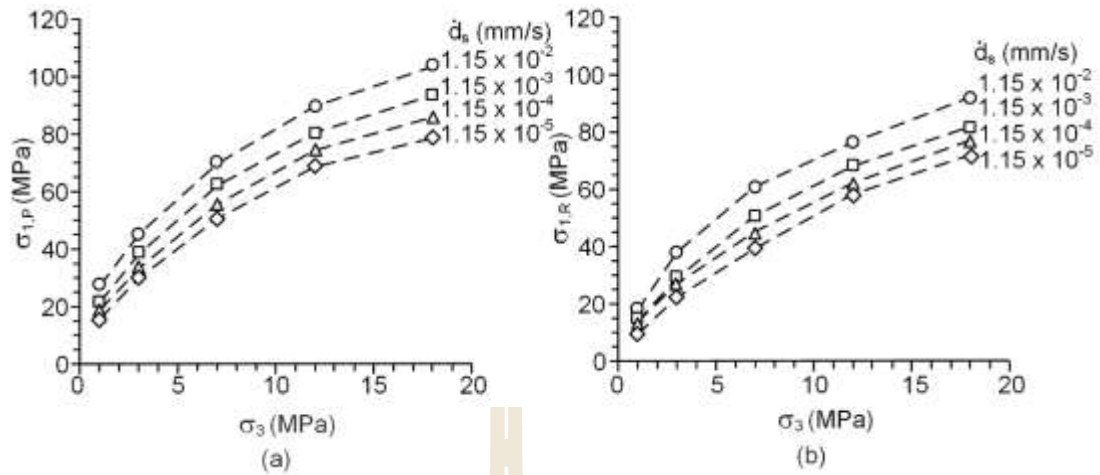
Figure 4.7 Major principal stresses at peak, $\sigma_{1,P}$ (a) and residual, $\sigma_{1,R}$ (b) as a function of confining stress (σ_3).

Dilation is the normal separation of the fracture and governed by the fracture roughness. In normal and shear displacements of the triaxial shear test as performed in this study can be calculated form the relative vertical and lateral displacements of the rock specimens. The effects of the confining stress (or normal stress) and shear velocity can be revealed from the d_n-d_s diagrams. The dilations tend to increase with the displacement until the peak stresses are reached, and remain constant in the residual region (Figure 4.8). Figure 4.9 shows that the dilation rates increase with the displacement velocity. The shear and normal (dilation) displacements of the tested fractures can be calculated using Eqs. (4.3) and (4.4). Figure 4.10 shows the maximum amplitudes of joint roughness coefficients (JRC) after testing for each confining pressure and shear velocity. Result shows that JRC trend to decrease with increasing displacement velocity and confining pressure.
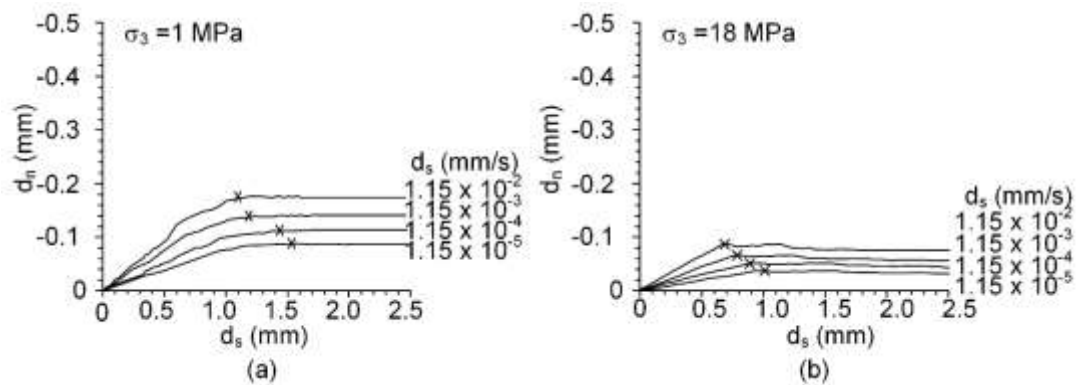
Figure. 4.8 Normal displacement d_n as a function of shear displacement d_s.
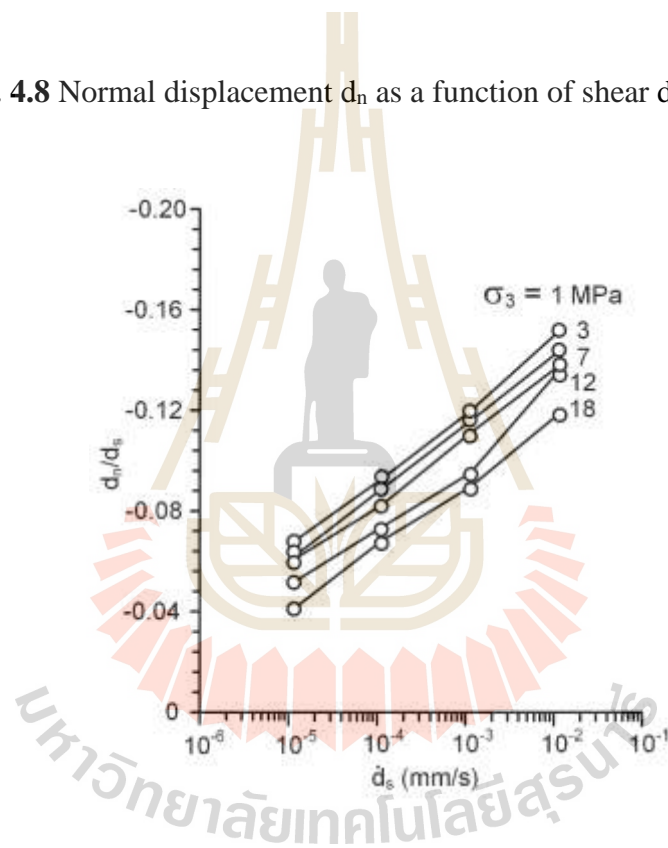
Figure. 4.9 Dilation rates (d_n/d_s) as a function of the shear velocity ($\dot{d_s}$).

Figure 4.11 shows examples of post-test fractures obtained under the highest and lowest displacement velocities and confining stresses. The light areas on the fracture surfaces represent the sheared-off asperities. Test result for the major principal strength (σ_1), shear strength (τ), normal strength (σ_n) cohesion (c) and friction angle (ϕ) for peak and residual shear strength on rough fracture listed in Tables 4.1
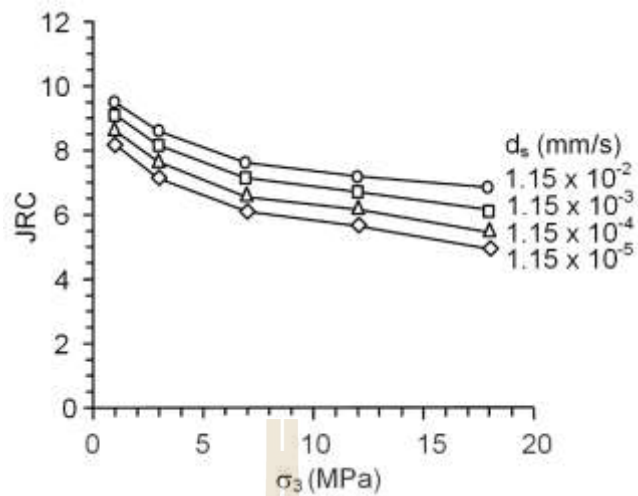
Figure 4.10 Joint roughness coefficient as a function of confining pressure (σ_3).

4.4 Test results on saw-cut fractures

Shear strengths testing on saw-cut fractures presented results in forms of shear stress as a function of normal stress show in Figure 4.12. Result show that basic friction angle (ϕ_b) becomes independent on shear velocity and constant at 31 degree. The result of triaxial shear test on saw-cut fracture under all displacement velocities and confining pressures are listed in Table 4.2

(d˙ₛ)

1.15×10^{-2} **mm/s**

(d˙ₛ)

1.15×10^{-5} **mm/s**

$\sigma_3 =$
1 MPa

3 MPa

7 MPa

12 MPa

18 MPa
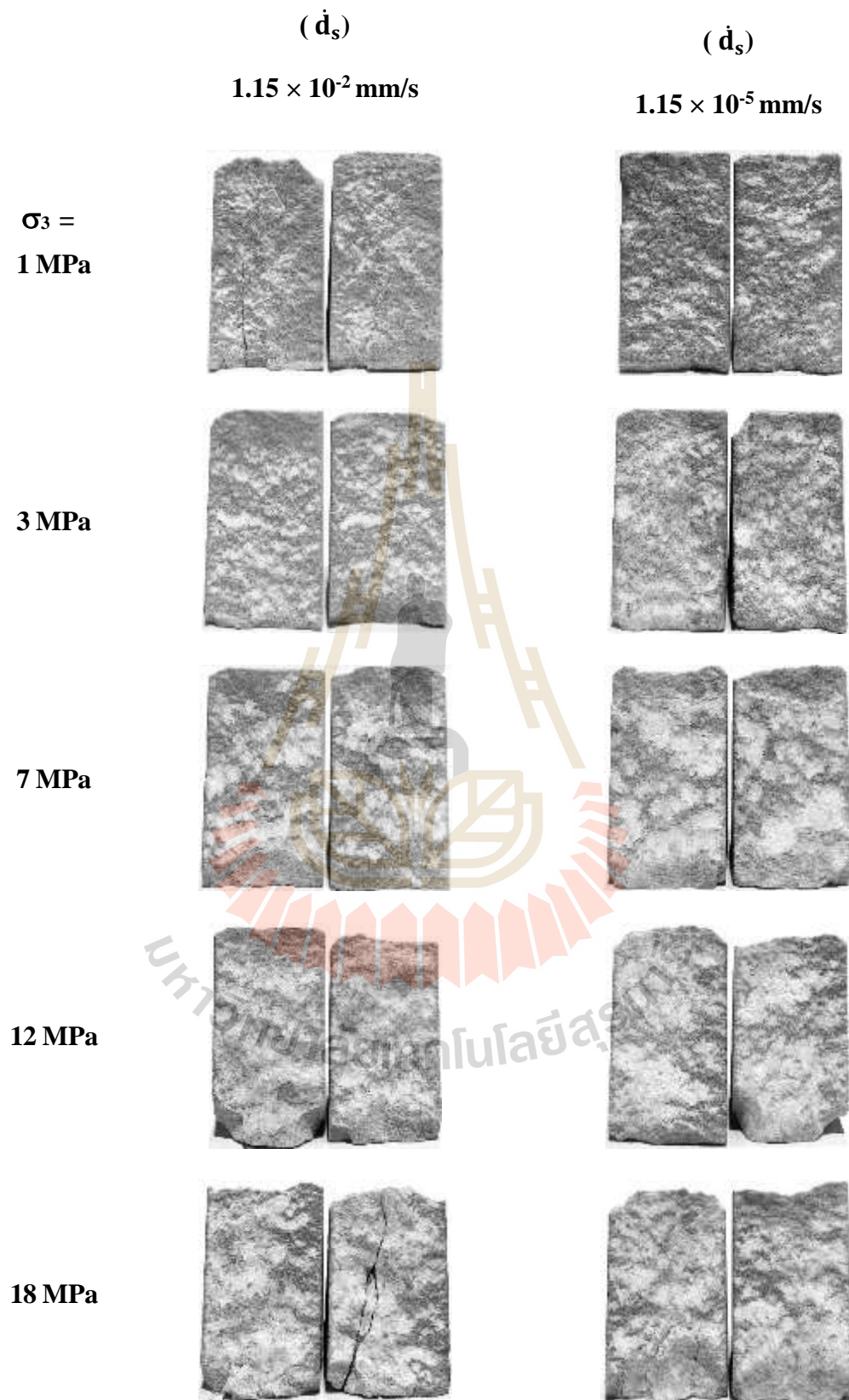
Figure 4.11 Some post-test rough fractures from triaxial shear test.

Table 4.1 Triaxial shear test result on rough fractures under all displacement velocities and confining pressures.

$\dot{d}_s$ (mm/s)	σ_3	Rough Fracture									
		Peak shear strength					Residual shear strength				
		σ_1 (Mpa)	τ_p (Mpa)	σ_n (Mpa)	c (Mpa)	ϕ (Degree)	σ_1 (Mpa)	τ_r (Mpa)	σ_n (Mpa)	c (Mpa)	ϕ (Degree)
1.15×10^{-2}	1	27.50	11.58	7.82			17.50	7.21	5.24		
	3	45.30	18.49	13.88			37.80	15.21	11.95		
	7	69.84	27.68	23.54	6.88	38.84	60.68	23.64	21.13	3.57	36.98
	12	89.56	34.16	32.42			76.23	28.29	28.91		
	18	103.49	37.65	40.51			91.82	32.51	37.43		
1.15×10^{-3}	1	21.67	9.03	6.32			13.33	5.39	4.17		
	3	38.63	15.57	12.17			28.63	11.20	9.59		
	7	62.34	24.37	21.57	5.74	37.78	50.68	19.24	18.50	2.07	35.93
	12	80.39	30.12	30.01			67.89	24.62	26.71		
	18	93.49	33.24	37.87			81.82	28.11	34.80		

Table 4.1 Triaxial shear test result on rough fractures under all displacement velocities and confining pressures. (continue)

$\dot{d}_s$ (mm/s)	σ_3	Rough Fracture Sat Condition									
		Peak shear strength					Residual shear strength				
		σ_1 (Mpa)	τ_p (Mpa)	σ_n (Mpa)	c (Mpa)	ϕ (Degree)	σ_1 (Mpa)	τ_r (Mpa)	σ_n (Mpa)	c (Mpa)	ϕ (Degree)
1.15x10⁻⁴	1	19.17	7.94	5.67	5.10	36.58	13.33	5.39	4.17	2.59	33.83
	3	33.63	13.39	10.88			26.96	10.47	9.17		
	7	55.68	21.44	19.81			44.84	16.67	16.96		
	12	74.56	27.55	28.47			62.06	22.05	25.18		
	18	85.99	29.94	35.90			76.82	25.90	33.49		
1.15x10⁻⁵	1	15.83	6.48	4.82	4.59	35.07	9.17	3.57	3.10	0.98	34.54
	3	30.30	11.93	10.02			21.96	8.29	7.88		
	7	50.68	19.24	18.50			39.01	14.10	15.43		
	12	68.73	24.98	26.93			57.89	20.21	24.08		
	18	78.49	26.64	34.16			71.82	23.70	32.41		
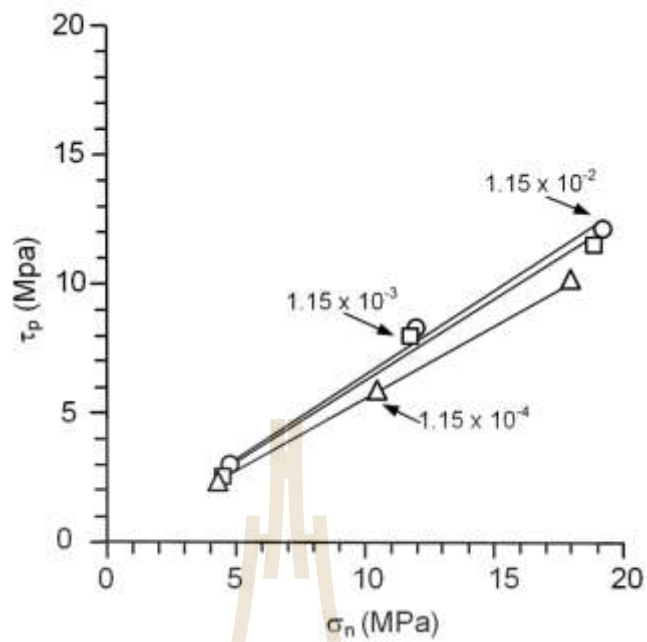
Figure 4.12 Peak shear strengths (τ_p) on saw-cut fracture as a function of normal
stress (σ_n).

Table 4.2 Results of triaxial shear tests on saw-cut fractures under all displacement
velocities and confining pressures.

$\dot{d}_s$ (mm/s)	σ_3	Saw-Cut Fracture					
		σ_1	τ_s	σ_n	c (MPa)	ϕ (Degree)	R^2
1.15x10⁻²	3	18.63	6.78	6.92	2.35	31	0.99
	7	30.68	10.43	13.23			
	12	47.89	15.70	21.25			
1.15x10⁻³	3	18.63	6.77	6.91	2.14	32	0.99
	7	29.01	9.69	12.79			
	12	47.89	15.81	21.45			
1.15x10⁻⁴	3	17.80	6.51	6.87	2.08	30	0.98
	7	27.34	8.86	12.17			
	12	45.39	14.46	20.35			

CHAPTER V

ANALYSIS OF RESULTS

5.1   Introduction

This chapter describes analysis of results from triaxial shear tests on tension-induced fractures and on smooth saw-cut surfaces. The results are used to developed strength criteria which would be useful for the prediction of fracture shear strengths under the boundary conditions beyond those used in this study. The contents include normalization of shear displacement rate, derivation of strength criteria for peak and residual regions, and isolation of effect of pore pressure from loading rate and the confining stress.

5.2   Normalization of shear displacement rate

Shear displacement rate tends to be enhanced under larger confining pressures. This is suggested by that the difference of the peak shearing resistance among different shear velocities tend to increase when the confining pressures are increased. The rate of shear displacements or shear velocity ($\dot{d}_s$) that are equivalent to axial displacement rate ($\dot{d}_1$) can be calculated using Eq. (4.3) as 1.15×10^{-5} to 1.15×10^{-2} mm/s. The ISRM suggested method (Muralha et al., 2014) specifies the shear velocity for the shear strength tests on rock fracture specimens in laboratory around $0.1–0.2$ mm/minute (2.5×10^{-3} mm/s) which are usually suitable for most conditions. To compare the strength results obtained under various shear rates with those of the ISRM suggested method.

The defined shear velocities must be normalized to isolate the shear velocity effect. The normalization of shear velocity can be made by dividing the " $\dot{d}_s$ " by shear velocity defined from the ISRM suggested method (2.5×10^{-3} mm/s).

5.3 Criterion for peak and residual shear strengths

The test results indicate that the shear strength at peak and residual regions under various shear velocities increase with normal stresses (Figure 5.1). The decreasing rate of the peak and residual stresses tend to be uniform with the changes of the order of the shear velocities. The non-linear behavior of the fracture is reflected as a curvature of shear-normal stresses relations. The upper bound of the shear strengths is defined by the angle β which is maintained constant at 60 degrees. The lower bound is defined by the basic friction angle (ϕ_b) obtained from the smooth saw-cut surfaces testing.
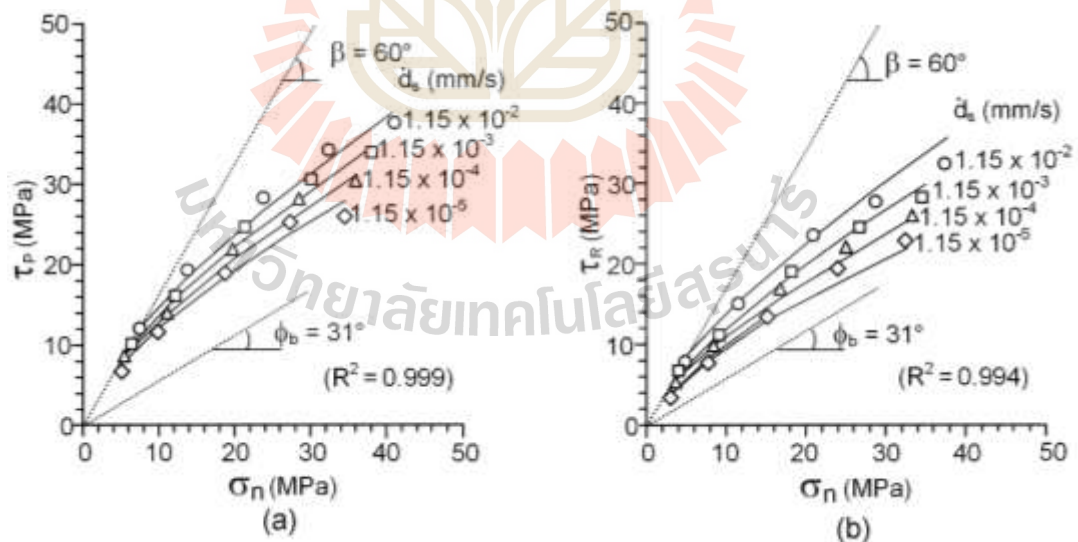
Figure 5.1 Comparison of empirical criterion with test data for peak, τ_P (a) and residual, τ_R (b) shear strengths.

An empirical equation is proposed to predict the shear strength at peak and residual shear strength as a function of normal stresses under saturated condition. Regression analyses are performed on equation. Good correlations are obtained ($R^2 > 0.9$)

$$\tau_P \text{ or } \tau_R = \alpha \sigma_n{}^\lambda \tag{5.1}$$

where τ_P is the shear strengths at peak, τ_R is the shear strengths at residual, α and λ are empirical parameters. The parameter α increases with shear velocity ($\dot{d}_s$), which can be best represented by:

$$\alpha = \eta \, \dot{d}_s{}^\omega \tag{5.2}$$

where η and ω are empirical constants, and $\dot{d}_s$ is shear displacements or shear velocity. Substituting Eq. (5.1) into (5.2) the shear strength at peak and residual as a function of normal stresses under various shear velocities can be obtained:

$$\tau_P \text{ or } \tau_R = \eta \, \dot{d}_s{}^\omega \sigma_n{}^\lambda \tag{5.3}$$

They are compared with those obtained by Kleepmek, et al. (2016) who conduct the same experiment on Phra Wihan sandstone under dry condition. The parameters α and λ determined for each shear velocity are summarized in Table 5.1. Their numerical values are given in Figure 5.2 which compares test data with curves fit of the proposed equation (5.3). This equation can be used to predict parameters of fractures under each confining. pressure. For both peak and residual, the parameter α for saturated sandstone is lower than those of the dry one.

Table 5.1 Empirical parameters α and λ at peak and residual shear strengths.

$\dot{d}_s$ (mm/s)		Peak		Residual	
		α	λ	α	λ
1.15×10^{-2}	This studies	3.05	0.686	2.67	2.25
	Kleepmek, et al. (2016)	3.31	0.700	2.74	0.721
1.15×10^{-3}	This studies	2.81	0.686	2.23	0.722
	Kleepmek, et al. (2016)	3.10	0.700	2.54	0.721
1.15×10^{-4}	This studies	2.64	0.686	2.16	0.722
	Kleepmek, et al. (2016)	2.90	0.700	2.36	0.721
1.15×10^{-5}	This studies	2.54	0.686	1.78	0.722
	Kleepmek, et al. (2016)	2.71	0.700	2.18	0.721

The parameter λ tends to be independent of the shear velocity. It probably relates to the fracture roughness. As a result for smooth saw-cut surface, λ would be equal to 1.0.
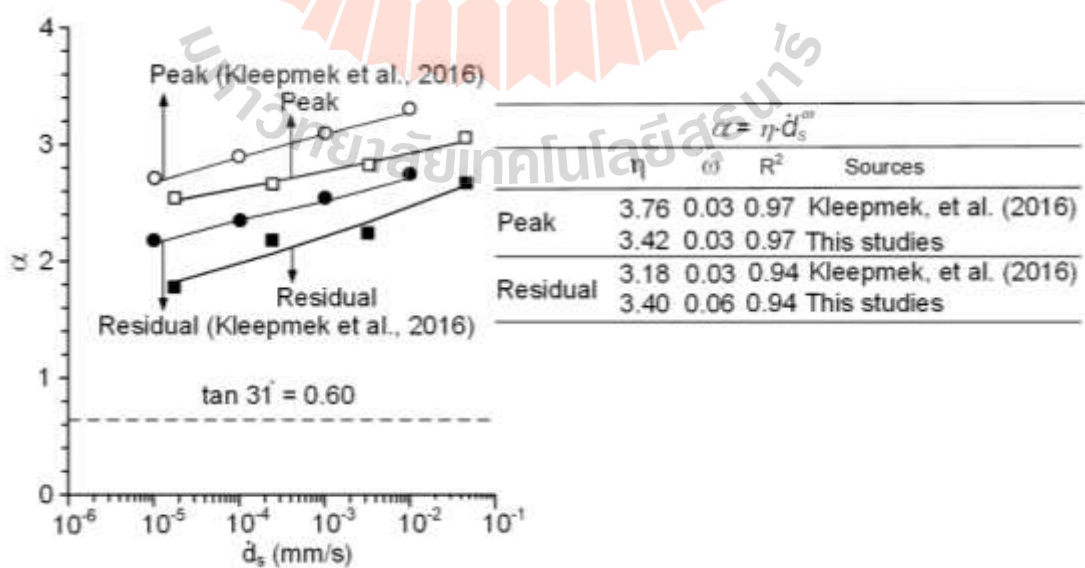
Figure 5.2 Empirical parameters α as a function of shear velocity.

5.4   Criterion for major principal stresses

The major principal stresses at peak and residual shear strengths under various shear velocities increase with confining stresses (Figure 5.3). The non-linear behavior of the fracture is reflected as a curvature of the major principal stress-confining stresses relations. An empirical equation is proposed to predict the major principal stresses at peak shear strength as a function of confining stresses:

$$\sigma_{1,P} \text{ or } \sigma_{1,R} = \varphi\sigma_3{}^{\varpi} \tag{5.4}$$

where $\sigma_{1,P}$ is major principal stresses at peak, $\sigma_{1,R}$ is major principal stresses at residual, φ and ϖ are empirical constants. Regressions analysis is performed to determine these parameters from the test data.
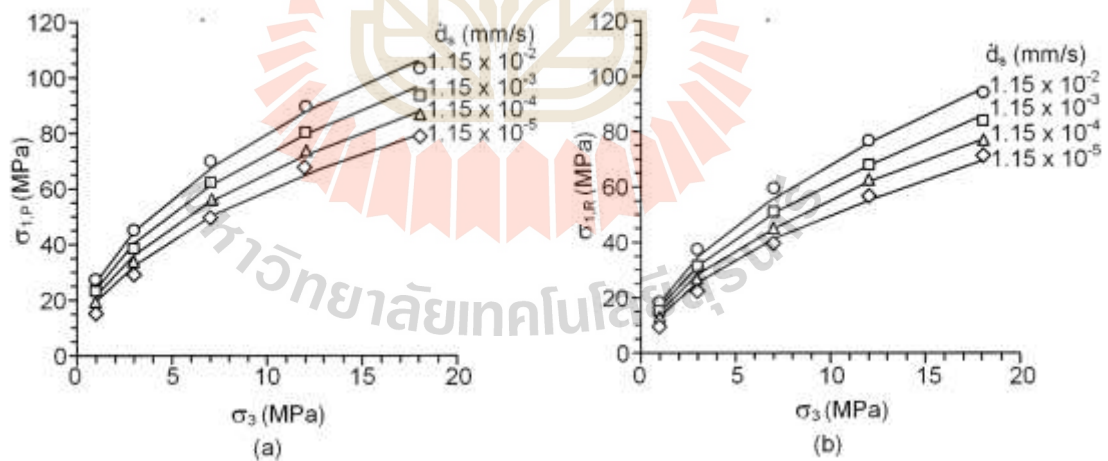
Figure 5.3 Major principal stresses at peak, $\sigma_{1,P}$ (a) and residual, $\sigma_{1,R}$ (b) as a function

of confining stress (σ_3).

The parameter ϖ tends to be independent of the shear velocity, but parameter φ increases with shear velocity ($\dot{d}_s$), which can be best represented by:

$$\varphi = \xi \ \dot{d}_s^{\ \iota} \tag{5.5}$$

where ξ and ι are empirical constants. Substituting Eq. (5.4) into (5.5) the major principal stress at peak and residual as a function of normal stresses under various shear velocities can be best represented by equation (5.6). Table 5.2 summarizes the calculation results. Good correlation is obtained ($R^2 > 0.9$).

$$\sigma_{1,\,P} \text{ or } \sigma_{1,\,R} = \xi \ \dot{d}_s^{\ \iota} \sigma_3^{\varpi} \tag{5.6}$$

This criterion can be used to predict fracture shear strength under various shear velocities in term of major principal stresses

5.5 Strength criterion based on strain energy density

The activation energy has been widely used for the predictions of fault movements at great depths (high confining pressures) (Stesky, 1978; Ohnaka, 1995; Odedra et al., 2001), where the fault dilation is neglected (i.e. plastic deformation of the shear zone).

Table 5.2 Empirical parameters φ and ϖ.

$\dot{d}_s$ (mm/s)	φ	ϖ	R^2
1.15×10^{-2}	28.200	0.46	0.997
1.15×10^{-3}	23.217	0.49	0.995
1.15×10^{-4}	20.038	0.51	0.994
1.15×10^{-5}	17.580	0.53	0.991

The strain energy density principle is applied here to describe the fracture strength and deformation under shear velocities. The distortional strain energy (W_d) required to displace the fractures can be defined as a function of mean strain energy (W_m) as follows:

$$W_d = \delta W_m + b \tag{5.7}$$

The parameters δ and b are empirical parameters. The strain energy criterion gives an advantage that both stress and strain at failure are incorporated to define the point at which the fracture can absorb the maximum energy before failure occurs. The distortional and mean strain energies can be calculated from the test results as: (Jaeger et al., 2007)

$$W_d = 3/2(\tau_{oct}/\gamma_{oct}) \tag{5.8}$$

$$W_m = 3/2(\sigma_m \cdot \varepsilon_m) \tag{5.9}$$

These are the normal stress, shear stress and strain that act on planes whose outward unit normal vectors, in the principal coordinate system. The normal stress, shear stress and strain acting on any octahedral plane is: (Jaeger et al., 2007)

$$\sigma_{oct} = (1/3)[\sigma_1{}^2 + \sigma_2{}^2 + \sigma_3{}^2]^{1/2} \tag{5.10}$$

$$\tau_{oct,} = [(1/3)[(\sigma_1 - \sigma_2)^2 + (\sigma_2 - \sigma_3)^2 + (\sigma_3 - \sigma_1)^2]]^{1/2} \tag{5.11}$$

$$\gamma_{oct} = [(1/3)[(\varepsilon_1 - \varepsilon_2)^2 + (\varepsilon_2 - \varepsilon_3)^2 + (\varepsilon_3 - \varepsilon_1)^2]]^{1/2} \tag{5.12}$$

$$\varepsilon_m = (1/3)[\varepsilon_1+\varepsilon_2+\varepsilon_3] \tag{5.13}$$

$$\sigma_m = (1/3)[\sigma_1+\sigma_2+\sigma_3] \tag{5.14}$$

where σ_{oct} = octahedral normal stress, τ_{oct} = octahedral shear stress, γ_{oct} = octahedral shear strain, ε_m = mean strain and σ_m = mean stress. Note that the strain parallel to the fracture strike is equal to zero because the test configurations do not allow lateral displacement in this direction. The octahedral normal and shear stresses have been calculated from equations (5.10) and (5.11). The octahedral shear stress of the fracture tends to increase with loading rate, and tends to be dependent of the confining pressure (Figure 5.4).
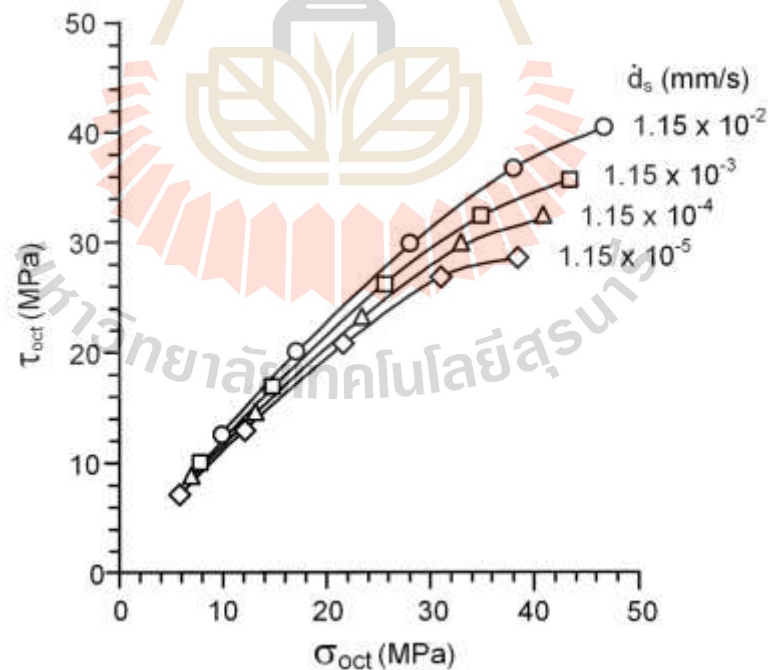
Figure 5.4 Octahedral shear stress (τ_{oct}) as a function of octahedral normal stress (σ_{oct}).

A linear relation between the distortional strain energy (W_d) and the mean strain energy (W_m) of the fractures is obtained. The W_d-W_m slope probably depends on the fracture roughness and strength of the asperities, which can be defined as a function of shear and mean strains and dilation of the fractures. Regression on the test results shows that the distortional strain energy increases linearly with the mean strain energy and with confining pressure, but independent of the loading rate. From test result the parameters δ and b are 1.30 and 0.02, which can be best represented by a linear relation in Figure 5.5. Results for the octahedral shear stresses ($\tau_{oct,f}$), octahedral shear strains ($\gamma_{oct,f}$), mean stress (σ_m), distortional strain energy density (W_d) and mean strain energy (W_m) at failure under are listed in Table 5.3.
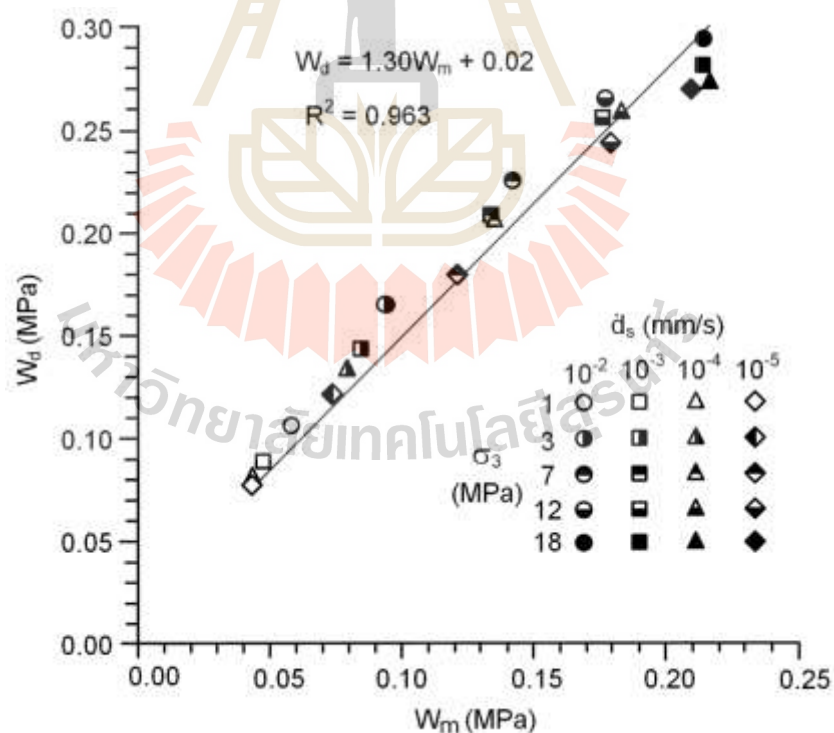
Figure 5.5 Distortional strain energy density (W_d) as a function of mean strain energy (W_m).

Table 5.3 Shear stress, strain and strain energy under various loading rates.

$\dot{d}_s$ (mm/s)	σ_3 (MPa)	τ_{oct} (MPa)	γ_{oct} (MPa)	σ_{oct} (MPa)	σ_m (MPa)	ε_m (MPa)	W_d (MPa)	W_m (MPa)
	1.0	12.5	0.0057	9.8	9.8	0.0039	0.1063	0.0579
	3.0	19.9	0.0055	17.1	17.1	0.0037	0.1646	0.0940
1.15×10^{-2}	7.0	29.6	0.0051	27.9	27.9	0.0034	0.2256	0.1415
	12.0	36.6	0.0048	37.9	37.9	0.0031	0.2654	0.1770
	18.0	40.3	0.0049	46.5	46.5	0.0031	0.2944	0.2142
	1.0	9.7	0.0061	7.9	7.9	0.0040	0.0891	0.0477
	3.0	16.8	0.0057	14.9	14.9	0.0038	0.1440	0.0841
1.15×10^{-3}	7.0	26.1	0.0053	25.4	25.4	0.0035	0.2088	0.1340
	12.0	32.2	0.0053	34.8	34.8	0.0034	0.2558	0.1765
	18.0	35.6	0.0053	43.2	43.2	0.0033	0.2816	0.2140
	1.0	8.6	0.0063	7.1	7.1	0.0041	0.0803	0.0434
	3.0	14.4	0.0062	13.2	13.2	0.0040	0.1332	0.0795
1.15×10^{-4}	7.0	22.9	0.0060	23.2	23.2	0.0039	0.2062	0.1352
	12.0	29.5	0.0058	32.9	32.9	0.0037	0.2578	0.1831
	18.0	32.0	0.0057	40.7	40.7	0.0035	0.2724	0.2165
	1.0	7.0	0.0075	5.9	5.9	0.0048	0.0787	0.0431
	3.0	12.9	0.0063	12.1	12.1	0.0041	0.1214	0.0736
1.15×10^{-5}	7.0	20.6	0.0058	21.6	21.6	0.0037	0.1795	0.1209
	12.0	26.7	0.0061	30.9	30.9	0.0039	0.2440	0.1788
	18.0	28.5	0.0059	38.2	38.2	0.0037	0.2700	0.2095

5.6 Effect of pore pressure

The effects of water saturation of the rock wall on the shearing behavior of fractures have rarely been addressed and experimentally investigated. Such condition may occur in rock embankments around the reservoir during drawdown and along roadways that subjected to long period of rainfall. Even though the water in fractures can be drained out

relatively quickly, the water in pore space of the rock hosting the fractures may influence the fracture shear strength. Results from this study suggest that the pore pressure has effect on the fracture shear strength if there is sufficient time to allow water to flow out of the specimens (Figure 5.6). Based on Coulomb criterion the cohesion and friction angle of the fractures are calculated. The cohesions and friction angles of the dry fractures and saturated fractures specimens are compared in Figures 5.7 and 5.8. The friction angles and cohesion under dry condition are higher than those of the saturated condition. They increase with displacement velocities. This may be due to the fact that rock asperities under saturation can be sheared-off more easily than those under dry condition.
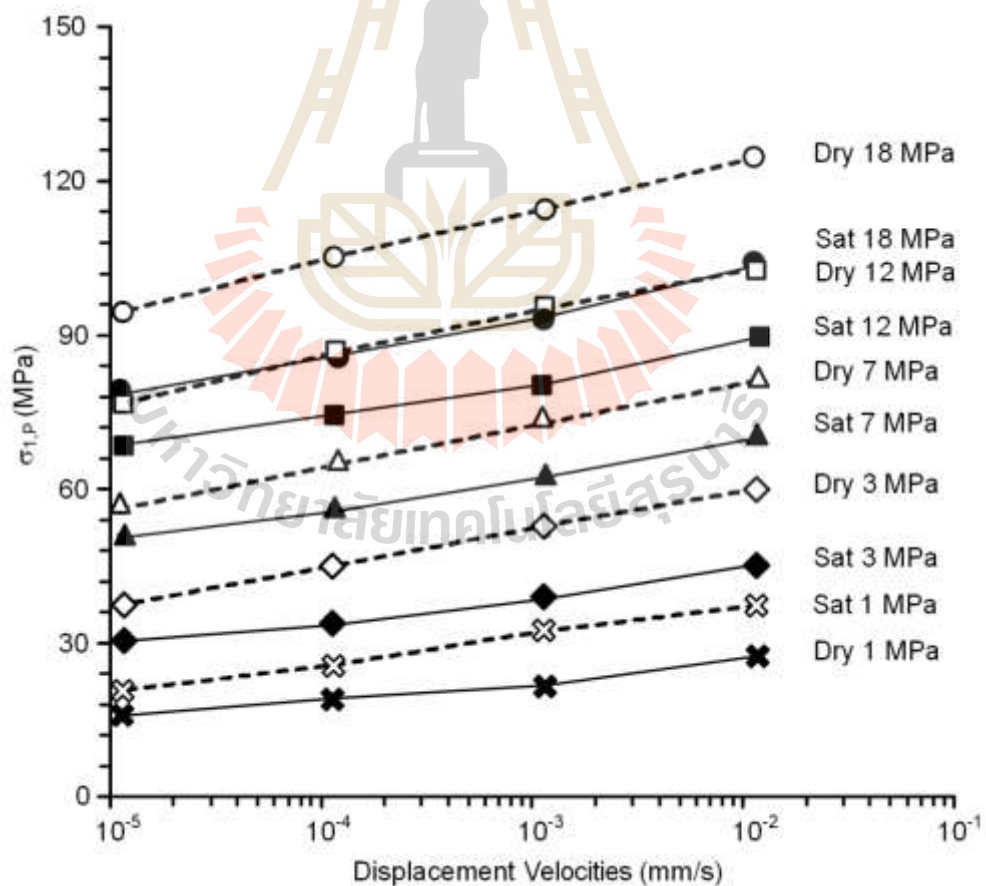
Figure 5.6 Major principal stress under dry condition (Kleepmek et al., 2016) and saturated condition (solid line) as a function of displacement velocity.
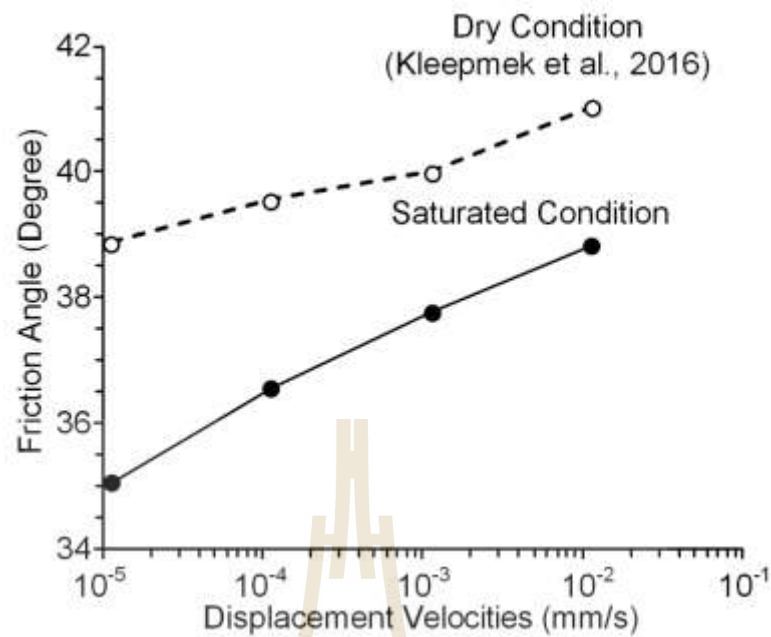
Figure 5.7 Friction angles under dry condition (Kleepmek et al., 2016) and saturated condition at a function of displacement velocities.
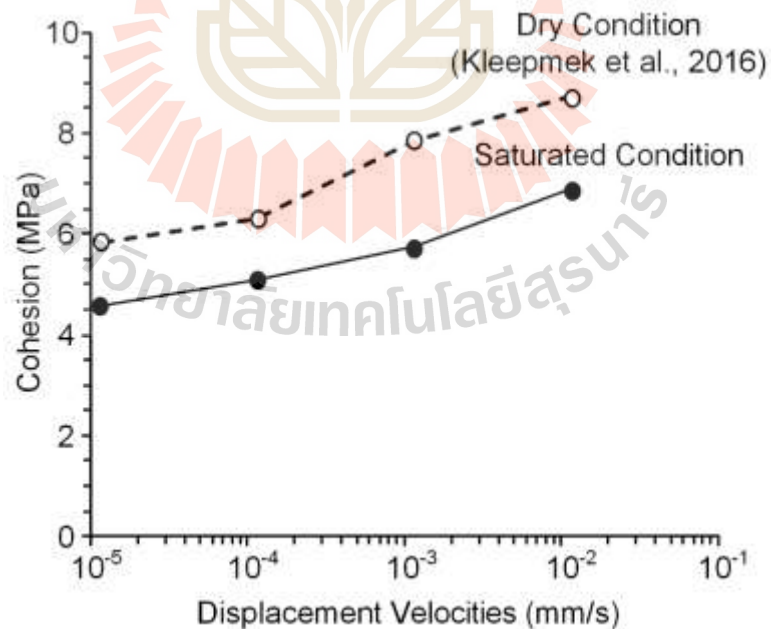
Figure 5.8 Cohesion under dry condition (Kleepmek et al., 2016) and saturated condition at a function of displacement velocities.

CHAPTER VI

DISCUSSIONS, CONCLUSIONS AND

RECOMMENDATIONS FOR FUTURE STUDIES

6.1 Discussions

All rock samples are rectangular block with nominal dimensions of $50 \times 50 \times 87$ mm^3 and the fracture areas are 100×50 mm^2 most suitable for the polyaxial loading device. Therefore the angle β which is maintained constant at 60°. This angle is primarily set because it yields the length to width ratio of the block specimens of about 2. Larger angles produce longer block specimen which can't be installed in the available device. It is believed that if the angle is reduced to below 45°, the shear sliding on the fractures may not occur. Instead the compression failure of the intact rock wedge would take place. The available polyaxial loading device can not apply confining stress σ_3 lower the 1 MPa. The test data under large confinements up to 18 MPa seem adequate and uniformly distributed. An assessment of the effect of fracture roughness on the response to the shear velocity can't be made. Only one degree of roughness (JRC) is obtained from the tension-inducing method. Nevertheless, the research findings clearly indicate that the rougher the fracture surface would show more effect from the shear velocity. This is also evidenced by that the shear strength of the smooth saw-cut surfaces is independent of the shear velocity.

It is recognized that increasing the number of the specimens under each confining stress and shear velocity would statistically enhance the reliability of the test

results and the predictability of the proposed strength criterion. Nevertheless, the results are adequately reliable, the measurement data conform reasonably well across the ranges of the test parameters (loading rates and confining stresses). Even though more samples are tested, they would not change the main conclusions drawn from this study.

6.2 Conclusions

The test results clearly show that the water saturation of the sandstone can reduce its fracture shear strengths. The fracture dilations measured prior and after the peak strengths significantly decrease with increasing confining pressures and decreasing displacement velocities. This is supported by the visual observations and the JRC measurements of the post-test fractures that the reduction of the shear velocity notably increases the sheared-off areas, particularly when the fractures are under high confining pressures. The τ-σ_n curves obtained under saturated condition tend to be lower than those obtained under dry condition obtained by Kleepmek et al. (2016), as suggested by the parameter α given in Figure 5.2. Under low loading rates the pore water is allowed to drain from the specimens, and hence the effect of pore pressure becomes lower. The effect of water saturation also acts more under high confining pressures. It tends to equally pronounced for all displacement velocities used in this test. This agrees reasonably well with the test results obtained by Khamrat et al. (2016) who found that the compressive strengths of the saturated Phra Wihan sandstone intact specimens were lower than those of the dry ones. The water saturation has no effect on the smooth saw-cut fracture. The basic friction angle obtained under saturation obtained here is similar to that obtained under dry condition by Kleepmek et al. (2016).

The parameter α would increase with increasing fracture roughness, as suggested by that the higher α is obtained under higher loading rate. For smooth fracture α will equal to $\tan\phi$ or about 0.601 for the tested sandstone. The parameter λ represents the non-linearity of the τ-σ_n curve. It would relate to the strength and roughness of the fractures. The results show definite trend in terms of the shear strengths as a function of normal stress for all shear velocities. The proposed empirical criterion also well fit to the test data as evidenced by the good correlation coefficients ($R^2 > 0.9$). Equations (5.1) and (5.2) can be used as strength criteria to assess the stability of fracture sandstone slope embankment under saturation. This would give more conservative results, as compared to those obtained by using the criterion derived from the dry condition testing. As evidenced by the good correlation coefficients obtained from the proposed empirical strength equation, test results are believed to be sufficiently reliable for all shear test results on rough and smooth fractures.

6.3 Recommendations for future studies

The uncertainties of the investigation and results discussed above lead to the recommendations for further studies as follows:

1. Performing tests on different rock types different porosity values to assess the effects of porosity with pore pressure.

2. Testing on larger fracture areas would provide a more representative of the shear strength results when they are applied to the actual fractures under in-situ condition.

3. It is desirable that fractures are prepared with larger angle β, as compared to the 60° used in this study to find the effect of the orientation of rock fractures that affects the shear strength.

4. Increasing the number of the specimens would statistically enhance the reliability of the test results and the predictability of the proposed strength criterion.

REFERENCES

ASTM D5607-08 (2008). **Standard test method for performing laboratory direct shear strength tests of rock specimens under constant normal force.** ASTM International West Conshohocken, PA.

Barton, N. and Choubey, V. (1977). The shear strength of rock joint in theory and practice. **Rock Mechanics.** 10(1–2): 1-54.

Barton, N. (1982). Characterizing rock masses to improve excavation design. Panel Report, Theme II Tunnelling and Excavation. In **Proceedings of fourth Congress IAEG**. New Delhi.

Barton, N. (2013). Shear strength criteria for rock, rock joints, rockfill and rock masses: Problems and some solutions. **Journal of Rock Mechanics and Geotechnical Engineering.** 5(4): 249-261.

Boonsener, M. and Sonpiron, K. (1997). Correlation of tertiary rocks in northeast, Thailand. In **Proceedings of International Conference on Stratigraphy and Tectonic Evolution of Southeast Asia and the South Pacific** (pp. 656-661). Bangkok, Thailand.

Brady, B.H.G. and Brown, E.T. (2006). **Rock Mechanics for Underground Mining**, Springer, Netherlands.

Curran, J.H. and Leoun, P.K. (1983). Influence of shear velocity on rock joint strength. In **Proceedings of International Congress on Rock Mechanics** (pp. 235-240). Melbourne.

Dyke, C.G. and Dobereiner, L. (1991). Evaluating the strength and deformability of sandstines. **Quarterly Journal of Engineering Geology.** 24: 123-134.

Fardin. N., Stephansson, O., and Jing, L. (2001). The scale dependence of rock joint surface roughness. **International Journal of Rock Mechanics and Mining Sciences.** 38: 659–669.

Fuenkajorn, K. and Kenkhunthod, N. (2010). Influence of loading rate on deformability and compressive strength of three Thai sandstones. **Geotechnical and Geological Engineering.** 28(5): 707-715.

Grasselli, G. and Egger, P. (2003). Constitutive law for the shear strength of rock joints based on three-dimensional surface parameters. **International Journal of Rock Mechanics & Mining Sciences.** 40(1): 25-40.

Hawkins, A.B. and McConnell, B.J. (1992). Sensitivity of sandstone strength and deforability to changes in moisture content. **Quarterly Journal of Engineering Geology.** 25: 115-130.

Jaeger, J.C., Cook, N.G.W., and Zimmerman, R.W., (2007). **Fundamentals of Rock Mechanics**. 475p.

Jiang, Y., Xiao, J., Tanabashi, Y., and Mizokami, T. (2004). Development of an automated servo-controlled direct shear apparatus applying a constant normal stiffness condition. **International Journal of Rock Mechanics and Mining Sciences.** 41: 275-286.

Kapang, P., Walsri, C., Sriapai, T., and Fuenkajorn, K. (2013). Shear strengths of sandstone fractures under true triaxial stresses. **Journal of Structural Geology.** 48: 57-71.

Fuenkajorn, K. and Kenkhunthod, N. (2010). Influence of loading rate on deformability and compressive strength of three Thai sandstones. **Geotechnical and Geological Engineering.** 28: 707–715.

Khamrat, S., Archeeploha, S., and Fuenkajorn, K. (2016). Pore pressure effects on strength and elasticity of ornamental stones. **Scienceasia.** 42: 121-135.

Kleepmek, M., Khamrat, S., Thongprapha, T., and Fuenkajorn, K. (2016). Displacement velocity effects on rock fracture shear strengths. **Journal of Structural Geology.** 90: 48-60.

Lee, H.S., Park, Y.J., Cho, T.F., and You, K.H. (2001). Influence of asperity degradation on the mechanical behavior of rough rock joints under cyclic shear loading. **International Journal of Rock Mechanics and Mining Sciences.** 38(7): 967-980.

Li, H.B., Zhao, J., and Li, T.J. (1999). Triaxial compression tests on a granite at different strain rates and confining pressures. **International Journal of Rock Mechanics and Mining Sciences.** 36: 1057-1063.

Li, Y., Wang, J., Jung, W., and Ghassemi, A. (2012). Mechanical properties of intact rock and fractures in welded tuff from Newberry volcano. In **Proceedings of Thirty-Seventh Workshop on Geothermal Reservoir Engineering**. California.

Morris, J.P. (2003). Review of rock joint models. **Lawrence Livermore National Laboratory Report**, UCR-ID-153650.

Muralha, J., Grasselli, G., Tatone, B., Blumel, M., Chryssanthakis, P., and Yujing, Y. (2014). ISRM Suggested Method for Laboratory

Determination of the Shear Strength of Rock Joints: Revised Version. **Rock Mechanics and Rock Engineering.** 47(1): 291-302.

Obert, L., Brady, B.T., and Schmechel, F. W. (1976). The effect of normal stiffness on the shear resistance of rock. **Rock Mechanics.** 8(2): 57-72.

Odedra, A., Ohnaka, M., Mochizuki, H., and Sammonds, P. (2001). Temperature and pore pressure effects on the shear strength of granite in the Brittle-Plastic Transition Regime. **Geophysical Research Letters.** 28(15): 3011-3014.

Ohnaka, M. (1995). A shear failure strength law of rock in the brittle-plastic transition regime. **Geophysical Research Letters.** 22(1): 25-28.

Patton, F.D. (1966). Multiple modes of shear failure in rock and related materials. **Ph.D. Thesis**, University of Illinois, Urbana.

Phueakphum, D., Fuenkajorn, K., and Walsri, C. (2013). Effects of intermediate principal stress on tensile strength of rocks. **International Journal of Fracture.** 181(2): 163-175.

Ramamurthy, T. and Arora, V.K. (1994). Strength predictions for jointed rocks in confined and unconfined states. **International Journal of Rock Mechanics and Mining Sciences & Geomechanics Abstracts.** 31(1): 9-22.

Ray, S. K., Sarkar, M., and Singh, T. N. (1999). Effect of cyclic loading and strain rate on the mechanical behaviour of sandstone. **International Journal of Rock Mechanics and Mining Sciences.** 36(4): 543-549.

Shrivastava, A.K. and Rao, K.S. (2009). Shear behaviour of jointed rock: A state of Art. In **Proceeding of the Indian Geotechnical Conferenc**e (pp. 245-249). Guntur.

Stesky, R.M. (1978). Rock Friction-Effect of Confining Pressure, Temperature, and Pore Pressure. **Pure and Applied Geophysics.** Vol. 116.

Torok, A. and Vasarhelyi, B. (2010). The influence of fabric and water content on selected rock mechanical parameters of travertine, examples from Hungary. **Engineering Geology.** 115: 237-245.

Trimmer, D., Bonner, B., Heard, H.C., and Duba, A. (1980). Effect of pressure and stress on water transport in intact and fractured gabbro and granite. **Journal of Geophysical Research: Solid Earth.** 85(B12): 7059-7071.

Vasarhelyi, B. (2003). Some observations regarding the strength and deformability of sandstones in case of dry and saturated conditions. **Bulletin of Engineering Geology and the Environment.** 62: 245-249.

Vasarhelyi, B. and Van, P. (2006). Influence of water content on the strength of rock. **Engineering Geology.** 84: 70-74.

Yilmaz, I. (2010). Influence of water content on the strength and deformability of gypsum. **International Journal of Rock Mechanics and Mining Sciences.** 42(2): 342-347.

BIOGRAPHY

Mister Pittawat Liabkrathok was born on December 22, 1994 in Nakhon Ratchasima Province, Thailand. He received his Bachelor's Degree in Engineering (Geotechnology) from Suranaree University of Technology in 2017. For his post-graduate, he continued to study with a Master's degree in Civil, Transportation and Geo-resources Engineering Program, Institute of Engineering, Suranaree University of Technology. During graduation, 2017-2019, he was a part time worker in position of research assistant at the Geomechanics Research Unit, Institute of Engineering, Suranaree University of Technology.